

A curvature-weighted spectral precursor to dissipation in decaying three-dimensional turbulence: robustness across initial conditions and viscosity effects

Satori Tsuzuki^{1,*}

¹Research Center for Advanced Science and Technology, The University of Tokyo

(Dated: January 21, 2026)

We investigate the robustness of a curvature-weighted spectral precursor to dissipation in freely decaying three-dimensional incompressible turbulence. Building on our recent work in *Physical Review Fluids* on the Taylor–Green vortex, we analyze direct numerical simulations using the curl-of-vorticity spectrum $|\nabla \times \omega|^2(k)$, equivalent to a k^4 -weighted energy spectrum for solenoidal flow. Extending the study across multiple initial conditions—multi-mode ABC flows, a randomized low-wavenumber ABC field, the Taylor–Green vortex, and the Kida–Pelz flow—we find a consistent temporal ordering: the characteristic time associated with the advance and saturation of the peak wavenumber of $|\nabla \times \omega|^2(k)$ precedes the dissipation-peak time, which in turn precedes the characteristic time associated with the peak scale of the nonlinear energy-flux spectrum. We further probe viscosity effects in Taylor–Green turbulence: the precursor persists at lower viscosity when adequate resolution is employed, but weakens and can break at higher viscosity, consistent with stronger viscous damping of curvature-dominated small-scale content. Throughout, we use explicit inspection of curvature-weighted spectra to distinguish physical peak evolution from cutoff-proximate artifacts. These results establish robustness across initial conditions and clarify the practical role of viscosity and resolution for deploying curvature-weighted spectral precursors in decaying turbulence.

I. INTRODUCTION

Predicting *when* a three-dimensional (3D) turbulent flow reaches its dissipation peak is central to both theory and practice. In freely decaying turbulence, the dissipation rate $\varepsilon(t)$ exhibits a pronounced transient maximum that reflects the formation of the smallest dynamically active scales. Accurate anticipation of this event is relevant not only for physical interpretation of nonequilibrium cascade development, but also for adaptive strategies in simulations and experiments, such as output scheduling and dynamic resolution control. Despite decades of progress, reliable *precursors* that provide actionable early warning of the dissipation surge remain limited, especially in transient, non-stationary settings.

A standard spectral description of turbulent transients relies on the energy spectrum $E(k)$, the enstrophy spectrum $Z(k) \propto k^2 E(k)$, and the cumulative nonlinear flux $\Pi(K)$ [1, 2]. In decaying flows, however, these observables do not always serve as sharp predictors of the imminent dissipation peak. For instance, inertial-range development in $E(k)$ can be gradual and sensitive to finite-resolution and finite-time effects [3, 4]. Flux-based indicators are more directly tied to interscale transfer, but the flux peak scale can exhibit an appreciable lag relative to small-scale formation and dissipation [5, 6]. In parallel, real-space visualizations (e.g., Q -criterion isosurfaces) often reveal morphological transitions from large-scale coherent structures to filament-dominated states [7, 8], but translating such observations into quantitative early-warning metrics is nontrivial.

In our recent Letter on the decaying Taylor–Green vor-

tex (TGV) [9], we introduced a small-scale weighted diagnostic based on the spectrum of the curl of vorticity. With $\omega = \nabla \times \mathbf{u}$, incompressibility $\nabla \cdot \mathbf{u} = 0$ implies $\nabla \times \omega = -\nabla^2 \mathbf{u}$, and therefore the isotropic spectrum of $|\nabla \times \omega|^2$ is equivalent to a k^4 -weighted energy spectrum,

$$|\nabla \times \omega|^2(k, t) = k^4 E(k, t), \quad (\nabla \cdot \mathbf{u} = 0), \quad (1)$$

where k denotes the (integer-binned) isotropic wavenumber. The corresponding peak wavenumber,

$$k_{\text{peak}}[|\nabla \times \omega|^2](t) \equiv \arg \max_{k \geq 1} \left\{ |\nabla \times \omega|^2(k, t) \right\}, \quad (2)$$

was found to advance rapidly to intermediate-small scales and then level off *before* the dissipation rate $\varepsilon(t) = \sum_k 2\nu k^2 E(k, t)$ reaches its maximum. Moreover, the characteristic time associated with this rapid advance precedes the time associated with the largest peak scale of $|\Pi(K)|$, yielding the robust ordering $t_k < t_\varepsilon < t_\Pi$ across 256^3 – 1024^3 resolutions for the TGV [9]. This behavior is physically consistent with the k^4 weighting: it accentuates the incipient formation of high-curvature sheets and tightly wound tubes, where viscosity ultimately acts most strongly.

A key open question, however, is whether this precursor is *universal* across substantially different initial conditions. The TGV is highly symmetric and has served as a canonical benchmark for the creation of small scales [3, 10, 11], but its symmetry may constrain the route to turbulence. To establish broader relevance, it is essential to test initial conditions that differ in topology, helicity content, and symmetry breaking. Equally important, the k^4 weighting in Eq. (1) can amplify high-wavenumber tails; at finite resolution, this can lead to spurious peak picking near the spectral cutoff unless detection robustness is carefully assessed. Such issues

* tsuzukisatori@g.ecc.u-tokyo.ac.jp

are typically mild for lower-order weights (e.g., $k^2 E(k)$), but become non-negligible for curvature-biased measures such as $|\nabla \times \boldsymbol{\omega}|^2(k)$.

In this work, we extend the precursor framework to a diverse suite of freely decaying 3D flows under a unified numerical and post-processing protocol. We perform pseudo-spectral direct numerical simulations at viscosity $\nu = 10^{-3}$ and base resolution 512^3 for five distinct initial conditions: (i) a multi-mode Arnold–Beltrami–Childress (ABC) flow, (ii) an asymmetric multi-mode ABC flow, (iii) an ABC flow augmented by a random-phase low- k perturbation, (iv) the TGV (as a reference), and (v) the Kida–Pelz flow, a classical configuration known to generate intense small-scale activity [3, 12, 13].

To assess peak-detection reliability in a stringent setting, we additionally perform a 1024^3 Kida–Pelz simulation, which provides a high-resolution reference and is used as the basis for extracting characteristic times for that initial condition. Across all initial conditions, we observe a consistent temporal ordering in which the characteristic time associated with the rapid advance of $k_{\text{peak}} [|\nabla \times \boldsymbol{\omega}|^2]$ precedes the dissipation-peak time, which in turn precedes the time associated with the largest peak scale of the nonlinear flux:

$$t_k < t_\varepsilon < t_\Pi. \quad (3)$$

We further show that the k^4 weighting can, at moderate resolution, produce cutoff-proximate peak locking in peak-based metrics (most clearly for the 512^3 Kida–Pelz run). Throughout this paper we therefore accompany peak-based results with explicit inspections of $|\nabla \times \boldsymbol{\omega}|^2(k)$ to verify that the detected maximum lies away from the analysis cutoff. When a cutoff-proximate peak is observed at 512^3 , we treat it as a resolution warning and rely on higher-resolution reference data to extract characteristic times (notably the 1024^3 Kida–Pelz run).

The remainder of the paper is organized as follows. Section II summarizes the governing equations, numerical method, and spectral post-processing conventions, including the definitions of $E(k)$, $D(k) = 2\nu k^2 E(k)$, the transfer $T(k)$, and the cumulative flux $\Pi(K)$. Section III describes the set of initial conditions and simulation parameters. Section IV introduces the characteristic times $(t_k, t_\varepsilon, t_\Pi)$ and details the robustness checks for peak detection specific to the k^4 -weighted diagnostic. Section V presents the main comparative results across initial conditions, including a summary table of $(t_k, t_\varepsilon, t_\Pi)$ and the corresponding lead/lag times. Section VI discusses physical interpretation and limitations, and Section VII concludes with implications and outlook.

II. GOVERNING EQUATIONS AND NUMERICAL METHOD

A. Governing equations

We consider freely decaying, incompressible turbulence governed by the 3D Navier–Stokes equations in a periodic box of size $L = 2\pi$:

$$\partial_t \mathbf{u} + (\mathbf{u} \cdot \nabla) \mathbf{u} = -\nabla p + \nu \nabla^2 \mathbf{u}, \quad (4)$$

$$\nabla \cdot \mathbf{u} = 0, \quad (5)$$

where $\mathbf{u}(\mathbf{x}, t)$ is the velocity, $p(\mathbf{x}, t)$ is the kinematic pressure, and ν is the kinematic viscosity. The vorticity is $\boldsymbol{\omega} = \nabla \times \mathbf{u}$. We use the volume average $\langle \cdot \rangle \equiv (2\pi)^{-3} \int_{[0, 2\pi)^3} (\cdot) d\mathbf{x}$. The kinetic energy and dissipation rate are

$$K(t) \equiv \frac{1}{2} \langle |\mathbf{u}|^2 \rangle, \quad \varepsilon(t) \equiv -\frac{dK}{dt} = \nu \langle |\nabla \mathbf{u}|^2 \rangle. \quad (6)$$

B. Pseudo-spectral direct numerical simulations

We solve Eqs. (4)–(5) using a massively parallel pseudo-spectral method with FFTW–MPI slabs and a real-to-complex layout [14]. The velocity field is represented by a Fourier series

$$\mathbf{u}(\mathbf{x}, t) = \sum_{\boldsymbol{\kappa}} \hat{\mathbf{u}}(\boldsymbol{\kappa}, t) e^{i\boldsymbol{\kappa} \cdot \mathbf{x}}, \quad \boldsymbol{\kappa} = (\kappa_x, \kappa_y, \kappa_z) \in \mathbb{Z}^3, \quad (7)$$

on an N^3 collocation grid. Spectral derivatives are computed exactly, e.g., $\partial_j u_i \leftrightarrow i\kappa_j \hat{u}_i$. The nonlinear term

$$\mathbf{N}(\mathbf{x}, t) \equiv (\mathbf{u} \cdot \nabla) \mathbf{u} \quad (8)$$

is assembled in physical space from u_i and the spectral derivatives, transformed to Fourier space, and then projected to enforce incompressibility. In Fourier space, the evolution for each mode can be written as

$$\partial_t \hat{\mathbf{u}}(\boldsymbol{\kappa}, t) = -\hat{\mathbf{N}}_\perp(\boldsymbol{\kappa}, t) - \nu |\boldsymbol{\kappa}|^2 \hat{\mathbf{u}}(\boldsymbol{\kappa}, t), \quad (9)$$

where $\hat{\mathbf{N}}_\perp(\boldsymbol{\kappa}, t) = \mathbf{P}(\boldsymbol{\kappa}) \hat{\mathbf{N}}(\boldsymbol{\kappa}, t)$, and \mathbf{P} is the Leray projector

$$\mathbf{P}(\boldsymbol{\kappa}) = \mathbf{I} - \boldsymbol{\kappa} \boldsymbol{\kappa}^\top / |\boldsymbol{\kappa}|^2, \quad (\boldsymbol{\kappa} \neq \mathbf{0}), \quad (10)$$

which removes pressure and enforces $\boldsymbol{\kappa} \cdot \hat{\mathbf{u}} = 0$ [2, 15].

Dealiasing is performed by the standard two-thirds rule in a *box* sense during time marching: Fourier coefficients are set to zero whenever any component satisfies $|\kappa_i| > N/3$. Time integration uses a classical fourth-order Runge–Kutta scheme with an integrating factor for the viscous term [16, 17]. Velocity and vorticity snapshots are written at regular intervals for post-processing; per-rank storage enables parallel I/O and exact reconstruction consistent with the FFTW–MPI decomposition.

C. Isotropic spectra, transfer, and flux

From saved snapshots we compute isotropic shell averages of the energy spectrum $E(k, t)$, the enstrophy spectrum $Z(k, t)$, the dissipation spectrum $D(k, t)$, and the curl-of-vorticity spectrum $|\nabla \times \boldsymbol{\omega}|^2(k, t)$. We denote the wavevector magnitude by $\kappa \equiv |\boldsymbol{\kappa}|$ and define the integer isotropic wavenumber by binning

$$k \equiv \text{round}(\kappa), \quad \mathcal{S}_k \equiv \{\boldsymbol{\kappa} : \text{round}(|\boldsymbol{\kappa}|) = k\}. \quad (11)$$

The shell-summed energy spectrum is defined such that $\sum_k E(k, t) = K(t)$:

$$E(k, t) = \frac{1}{2} \sum_{\boldsymbol{\kappa} \in \mathcal{S}_k} |\hat{\mathbf{u}}(\boldsymbol{\kappa}, t)|^2. \quad (12)$$

Similarly,

$$Z(k, t) = \frac{1}{2} \sum_{\boldsymbol{\kappa} \in \mathcal{S}_k} |\hat{\boldsymbol{\omega}}(\boldsymbol{\kappa}, t)|^2 = k^2 E(k, t), \quad (13)$$

and the dissipation spectrum is

$$D(k, t) = 2\nu k^2 E(k, t), \quad \varepsilon(t) = \sum_k D(k, t). \quad (14)$$

For incompressible flow, $\nabla \times \boldsymbol{\omega} = -\nabla^2 \mathbf{u}$ implies the equivalence

$$|\nabla \times \boldsymbol{\omega}|^2(k, t) = \frac{1}{2} \sum_{\boldsymbol{\kappa} \in \mathcal{S}_k} |\widehat{\nabla \times \boldsymbol{\omega}}(\boldsymbol{\kappa}, t)|^2 = k^4 E(k, t), \quad (15)$$

which motivates the k^4 -weighted diagnostic emphasized in this work.

To quantify interscale transfer we compute the transfer function directly from modal transfers in Fourier space:

$$T(k, t) = - \sum_{\boldsymbol{\kappa} \in \mathcal{S}_k} \Re \left\{ \hat{\mathbf{u}}^*(\boldsymbol{\kappa}, t) \cdot \hat{\mathbf{N}}_\perp(\boldsymbol{\kappa}, t) \right\}, \quad (16)$$

where $\mathbf{N} = (\mathbf{u} \cdot \nabla) \mathbf{u}$ and $\hat{\mathbf{N}}_\perp$ is defined in (9)–(10). The cumulative flux is reported as

$$\Pi(K, t) = - \sum_{m \leq K} T(m, t), \quad (17)$$

so that $\Pi(K_{\max}, t) \approx 0$ and $\sum_k T(k, t) \approx 0$ provide discrete conservation diagnostics (up to round-off).

For the post-processing of isotropic spectra and transfer/flux, we apply a *spherical* two-thirds analysis mask and record it as a binary column `mask` in the spectra output; unless stated otherwise, all shell sums, peak searches, and plots are restricted to shells with `mask`=1. The mask keeps only modes with $\kappa \leq K_{\text{cut}} \equiv [(2/3)K_{\max}]$ (with $K_{\max} = N/2$) and therefore differs from the *box* two-thirds cutoff enforced during time marching. Because FFTW stores only half of the spectrum in the real-to-complex layout, contributions are

weighted so that the $k_z = 0$ and Nyquist planes carry a unit weight while the remaining planes carry weight 2, ensuring exact counting of conjugate pairs. With our FFT normalization, $\sum_k E(k, t)$ is equal to the volume-averaged kinetic energy $K(t)$. We accumulate shell sums using Kahan summation to reduce floating-point cancellation [18].

III. INITIAL CONDITIONS AND SIMULATION SET

A. Initial conditions

We compare five freely decaying incompressible flows, each initialized in the periodic box $[0, 2\pi]^3$. The cases are designed to span markedly different symmetries and large-scale organizations: a canonical nonhelical benchmark (TGV), helical structured flows (ABC-based), an ABC flow with an additional random-phase low- k component, and a classical high-symmetry configuration known to generate intense small-scale activity (Kida–Pelz). Unless otherwise noted, all initial fields have zero spatial mean, and the subsequent evolution is purely decaying (no forcing).

ABC building block. Our ABC-type initial conditions are constructed from the generalized Arnold–Beltrami–Childress (ABC) form

$$\begin{aligned} \mathbf{u}_{\text{ABC}}(x, y, z; A, B, C; k_x, k_y, k_z) \\ = \begin{bmatrix} A \sin(k_z z) + C \cos(k_y y) \\ B \sin(k_x x) + A \cos(k_z z) \\ C \sin(k_y y) + B \cos(k_x x) \end{bmatrix}, \end{aligned} \quad (18)$$

which reduces to the classical ABC flow when $A = B = C = 1$ and $k_x = k_y = k_z = 1$ in a 2π -periodic domain. In all ABC-based cases below, we set $A = B = C = 1$ for each ABC component and vary only the integer wavenumber triplets and superposition weights.

(a) Multi-ABC. The multi-mode ABC case is the superposition of two ABC components,

$$\begin{aligned} \mathbf{u}(x, y, z, 0) = & w_1 \mathbf{u}_{\text{ABC}}(x, y, z; 1, 1, 1; 1, 1, 1) \\ & + w_2 \mathbf{u}_{\text{ABC}}(x, y, z; 1, 1, 1; 2, 2, 2), \end{aligned} \quad (19)$$

with weights $(w_1, w_2) = (1.0, 0.5)$. After the superposition, the field is rescaled to a target kinetic energy (see below) to facilitate consistent comparisons of amplitude-based diagnostics.

(b) Multi-ABC (Asymmetric). To break the symmetry of the secondary ABC component, we replace the second wavenumber triplet in (19) by an asymmetric choice,

$$\begin{aligned} \mathbf{u}(x, y, z, 0) = & w_1 \mathbf{u}_{\text{ABC}}(x, y, z; 1, 1, 1; 1, 1, 1) \\ & + w_2 \mathbf{u}_{\text{ABC}}(x, y, z; 1, 1, 1; 2, 1, 3), \end{aligned} \quad (20)$$

again using $(w_1, w_2) = (1.0, 0.5)$, followed by the same energy rescaling.

(c) *ABC + random-phase low- k .* To test robustness against low-wavenumber randomness while retaining a structured large-scale backbone, we superpose an ABC field with a divergence-free random-phase perturbation supported only on low wavenumbers:

$$\mathbf{u}(x, y, z, 0) = w_{\text{abc}} \mathbf{u}_{\text{ABC}}(x, y, z; 1, 1, 1; 1, 1, 1) + w_{\text{rnd}} \mathbf{u}_{\text{rnd}}(x, y, z; k_{\text{max}}^{\text{rnd}}), \quad (21)$$

where $w_{\text{abc}} = 1.0$, $w_{\text{rnd}} = 0.3$, and $k_{\text{max}}^{\text{rnd}} = 3$. The random field \mathbf{u}_{rnd} is generated in Fourier space using random phases, projected to satisfy incompressibility mode-by-mode, and transformed back to physical space. A fixed seed is used for reproducibility (seed = 42). As in the multi-ABC cases, the combined field is rescaled to the target kinetic energy.

(d) *Taylor–Green vortex (TGV).* As a reference, we use the standard Taylor–Green initial condition [3, 10, 11]

$$\mathbf{u}(x, y, z, 0) = (\sin x \cos y \cos z, -\cos x \sin y \cos z, 0). \quad (22)$$

(e,f) *Kida–Pelz.* We use the standard high-symmetry Kida–Pelz initial condition [12, 13],

$$\begin{aligned} u_x(x, y, z, 0) &= A_{\text{KP}} \sin x (\cos 3y \cos z - \cos y \cos 3z), \\ u_y(x, y, z, 0) &= A_{\text{KP}} \sin y (\cos 3z \cos x - \cos z \cos 3x), \\ u_z(x, y, z, 0) &= A_{\text{KP}} \sin z (\cos 3x \cos y - \cos x \cos 3y), \end{aligned} \quad (23)$$

with a global amplitude factor A_{KP} . In the present simulations we set $A_{\text{KP}} = 1.0$. We perform two simulations for this initial condition: a base-resolution run at 512^3 (case (e)) and a higher-resolution run at 1024^3 (case (f)) used to assess the robustness of peak detection for the k^4 -weighted diagnostic (details in Sec. IV).

B. Simulation parameters and data output

The baseline set of simulations (cases (a)–(f)) is performed in the periodic domain $[0, 2\pi]^3$ at viscosity $\nu = 10^{-3}$. To probe viscosity dependence in a controlled setting, we additionally repeat the Taylor–Green vortex (TGV) initial condition at a lower viscosity $\nu = 2.5 \times 10^{-4}$ and at a higher viscosity $\nu = 10^{-2}$ (see Sec. VF). The base resolution is $N^3 = 512^3$ for cases (a)–(e) and for the high-viscosity TGV run, while companion $N^3 = 1024^3$ runs are performed for Kida–Pelz (case (f)) and for the low-viscosity TGV run in order to avoid cutoff-proximate peak locking in curvature-weighted spectra. Time integration uses a fixed time step $\Delta t = 10^{-3}$. Velocity (and, when needed, vorticity) snapshots are saved every $n_{\text{out}} = 50$ time steps for post-processing, corresponding to an output interval $\Delta t_{\text{out}} = 5 \times 10^{-2}$. The same spectral post-processing pipeline is applied to all cases (Sec. II), including the isotropic shell averaging conventions, the spherical two-thirds analysis mask, and transfer/flux diagnostics.

Because our focus is on timing relations and relative lead/lag measures, we choose the final integration time t_{end} in each case so that the dissipation episode is fully captured and the subsequent decay is sufficiently sampled. Specifically, we integrate up to $t_{\text{end}} = 60$ for the multi-ABC cases (a,b), $t_{\text{end}} = 120$ for the ABC+random low- k case (c), and $t_{\text{end}} = 20$ for the baseline TGV and Kida–Pelz runs (d–f). For the viscosity-variation TGV runs, we integrate up to $t_{\text{end}} = 16$ for $\nu = 2.5 \times 10^{-4}$ and up to $t_{\text{end}} = 12$ for $\nu = 10^{-2}$.

For cross-case comparisons of amplitude-based quantities derived from spectra (e.g., $\varepsilon(t)$ and scale measures), we adopt the same calibration convention as in Ref. [9]: the spectra are rescaled such that the total kinetic energy at the first post-processed snapshot equals a reference value $K_0 = 1/8$. This calibration does not affect peak wavenumbers such as $k_{\text{peak}}[|\nabla \times \omega|^2]$, and therefore does not alter the temporal ordering statements central to this work.

Qualitative flow evolution in the Q -criterion visualizations. Figures 1–5 show representative snapshots of the flow evolution for the five 512^3 simulations. In each panel, we plot an isosurface of the Q -criterion (with the same visualization settings as in Ref. [9]) and color it by the local speed $|\mathbf{u}|$. The sequences in the upper rows (a)–(h) are chosen to span the transient from the initial large-scale organization to the subsequent volume-filling turbulent state and late-time decay (note that the physical time windows differ across cases, reflecting the different characteristic time scales of each initial condition).

For the multi-mode ABC case [Fig. 1(a)–(h)], the initial field is dominated by smooth, domain-spanning structures characteristic of the superposed ABC modes. As time increases, these structures rapidly fragment into twisted ribbons and then proliferate into a dense tangle of slender tube-like features that progressively occupies the full domain, indicating vigorous small-scale generation during the dissipation episode. The asymmetric multi-mode ABC case [Fig. 2(a)–(h)] exhibits a qualitatively similar transition, while the broken symmetry yields a more heterogeneous spatial distribution and a less regular large-scale organization, with intermittent clustering of intense structures.

The ABC+random-phase low- k case [Fig. 3(a)–(h)] displays a noticeably slower route to a volume-filling tangle. Coherent, large-scale structures persist over a longer time interval, and the filamentary/tubular population becomes dense only at later times compared with the purely structured ABC-based cases, consistent with the delayed dissipation activity observed in the time-series diagnostics.

For the TGV [Fig. 4(a)–(h)], we recover the canonical progression from large-scale vortical sheets to rolled-up and interacting structures and finally to a densely tangled state, consistent with prior studies and our recent PRF Letter [9]. The Kida–Pelz case [Fig. 5(a)–(h)] develops intense small-scale structures very rapidly. Within a short time, the flow transitions from the highly sym-

metric initial arrangement to a domain-filling network of tightly curved tubes and sheets, underscoring the well-known propensity of this configuration to generate strong gradients [12, 13].

The lower panels (i) and onward in Figs. 1–5 annotate additional snapshots at characteristic times extracted from the spectral diagnostics, including t_k (the time at which the peak scale $k_{\text{peak}}[|\nabla \times \boldsymbol{\omega}|^2](t)$ attains its maximum), auxiliary reaching-time markers based on more global wavenumber measures (e.g., t_c and t_{95}), as well as the dissipation- and flux-related times t_ε and t_Π . These times are defined precisely and analyzed quantitatively in Secs. IV and V, where we establish their consistent temporal ordering across initial conditions. For the Kida–Pelz flow, the characteristic-time analysis reported below refers to the 1024^3 simulation (Sec. IV F and Table I); the 512^3 visualization in Fig. 5 is retained to highlight the rapid emergence of fine-scale structures and the resolution sensitivity of peak picking in curvature-weighted spectra.

IV. SPECTRAL DIAGNOSTICS AND CHARACTERISTIC TIMES

A. Isotropic spectra and calibration of the energy scale

From the stored velocity snapshots, we construct isotropic (shell-summed) spectra in the periodic cube $[0, 2\pi]^3$. As in our PRF Letter [9], shells are formed by binning Fourier modes by the integer $k = \text{round}(|\boldsymbol{\kappa}|)$ and accumulating plane-weighted sums appropriate for real-to-complex FFT layouts. For the analysis, we additionally apply a *spherical* two-thirds mask and record it as a binary column `mask` in the spectra output (we restrict sums and peak searches to shells with `mask`=1 unless stated otherwise). We denote the maximum retained shell by

$$k_{\text{max}}^{(\text{mask})} \equiv \max\{k : \text{mask}(k) = 1\}, \quad (24)$$

which corresponds to the familiar spherical two-thirds cutoff (for $N = 512$, $k_{\text{max}}^{(\text{mask})} = 171$).

To enable a consistent comparison across different initial conditions, we use a constant calibration factor α that rescales the spectra so that the total kinetic energy at the earliest stored time matches a target value K_0 :

$$\alpha = \frac{K_0}{\sum_k E(k, t_0)}, \quad E(k, t) \leftarrow \alpha E(k, t). \quad (25)$$

In the present study we take $K_0 = 1/8$, which coincides with the standard unit-amplitude TGV energy in $[0, 2\pi]^3$. All derived quantities below (including ε , η , and R_λ) are computed consistently from the calibrated spectra.

B. Spectral quantities: $E(k)$, $D(k)$, $\Pi(K)$, and $|\nabla \times \boldsymbol{\omega}|^2(k)$

We track the standard spectral diagnostics of decaying turbulence: the kinetic energy spectrum $E(k, t)$, the dissipation density

$$D(k, t) = 2\nu k^2 E(k, t), \quad (26)$$

and the dissipation rate

$$\varepsilon(t) = \sum_k D(k, t) = 2\nu \sum_k k^2 E(k, t). \quad (27)$$

We also analyze the nonlinear transfer spectrum $T(k, t)$ and the cumulative flux

$$\Pi(K, t) = - \sum_{m \leq K} T(m, t), \quad (28)$$

so that $|\Pi(K, t)|$ measures the magnitude of interscale transfer across the wavenumber K .

The central object of this work is the spectrum of the curl of vorticity,

$$|\nabla \times \boldsymbol{\omega}|^2(k, t), \quad \boldsymbol{\omega} \equiv \nabla \times \mathbf{u}, \quad (29)$$

which is strongly biased toward small scales. For incompressible flow, $\nabla \cdot \mathbf{u} = 0$ implies $\nabla \times \boldsymbol{\omega} = -\nabla^2 \mathbf{u}$, and therefore

$$|\nabla \times \boldsymbol{\omega}|^2(k, t) = k^4 E(k, t), \quad (30)$$

i.e., a k^4 -weighted energy spectrum. This k^4 weighting accentuates the incipient formation of high-curvature structures (tightly wound tubes and rolled-up sheets), which, as we show below, advances and saturates in wavenumber before $\varepsilon(t)$ reaches its maximum.

C. Integral and small-scale measures: L_{int} , λ , η , R_λ , and $k_{\text{max}} \eta$

We monitor four complementary measures of the evolving length scales. First, the instantaneous Kolmogorov scale is

$$\eta(t) = (\nu^3 / \varepsilon(t))^{1/4}. \quad (31)$$

Second, the integral scale is evaluated from the isotropic spectrum as

$$L_{\text{int}}(t) = \frac{\pi}{2 \sum_k E(k, t)} \sum_{k \geq 1} \frac{E(k, t)}{k}, \quad (32)$$

which emphasizes the energy-containing range. Third, the Taylor microscale is computed as

$$\lambda(t) = \left(\frac{\sum_k E(k, t)}{\sum_k k^2 E(k, t)} \right)^{1/2}, \quad (33)$$

and with $u'(t) = \sqrt{\frac{2}{3} \sum_k E(k, t)}$ we define the Taylor-scale Reynolds number

$$R_\lambda(t) = \frac{u'(t) \lambda(t)}{\nu}. \quad (34)$$

Finally, to quantify resolution, we track the standard criterion $k_{\max} \eta(t)$, where we follow Ref. [9] and define the maximum wavenumber by the Nyquist value $k_{\max} = (N/2) 2\pi/L$ (thus $k_{\max} = N/2$ in our $L = 2\pi$ domain). In Fig. 6 we plot $R_\lambda(t)$ together with $k_{\max} \eta(t)$. All cases satisfy $k_{\max} \eta(t) \gtrsim \mathcal{O}(1)$ throughout the time intervals analyzed, and the minimum typically occurs near the dissipation peak. Figure 7 summarizes the concurrent evolution of $L_{\text{int}}(t)$, $\lambda(t)$, $\eta(t)$, and $\varepsilon(t)$, highlighting that $\eta(t)$ reaches its minimum at $t = t_\varepsilon$ while the large-scale measures evolve more gradually.

D. k -metrics for spectral “peak scales”: peak, centroid, and quantiles

To quantify how far toward small scales a given diagnostic has progressed, we introduce several k -metrics for a nonnegative shell spectrum $S(k, t)$. The most direct measure is the peak wavenumber

$$k_{\text{peak}}[S](t) \equiv \arg \max_{k \geq k_{\min}} S(k, t), \quad (35)$$

where we take $k_{\min} = 1$. We also use the centroid scale

$$k_{\text{centroid}}[S](t) \equiv \frac{\sum_k k S(k, t)}{\sum_k S(k, t)}, \quad (36)$$

and the weighted quantile scale $k_q[S](t)$ defined by the cumulative weight:

$$k_q[S](t) \equiv \min \left\{ k : \frac{\sum_{m \leq k} S(m, t)}{\sum_m S(m, t)} \geq q \right\}, \quad 0 < q < 1. \quad (37)$$

In particular, we will refer frequently to $k_{95}[S](t)$.

In the present work, we apply these definitions to two spectra:

1. $S(k, t) = |\nabla \times \omega|^2(k, t)$ (the k^4 -weighted energy spectrum), and
2. $S(k, t) = |\Pi(k, t)|$ (the magnitude of the cumulative flux).

Figures 9–14 show the time evolution of the corresponding k -metrics for all cases: (a) Multi-ABC, (b) Multi-ABC (Asymmetric), (c) ABC + random-phase low- k , (d) TGV, (e) Kida–Pelz, and (f) Kida–Pelz [1024³], together with $\varepsilon(t)$. Across initial conditions, the different definitions (peak/centroid/quantile) yield consistent qualitative trends, with the peak metric providing the most direct “advance-and-level-off” indicator.

E. Characteristic times: t_ε , t_k , and t_Π

We define the dissipation peak time as

$$t_\varepsilon \equiv \arg \max_t \varepsilon(t). \quad (38)$$

For the peak-based diagnostics, we define the characteristic times by the maximum-attainment times of the peak scales:

$$t_k \equiv \arg \max_t k_{\text{peak}}[|\nabla \times \omega|^2](t), \quad (39)$$

$$t_\Pi \equiv \arg \max_t k_{\text{peak}}[|\Pi|](t). \quad (40)$$

When the maximum is attained over multiple consecutive outputs (a plateau), we take the earliest occurrence. For the TGV this is consistent with the “advance-and-level-off” onset time used in our Letter, because the rise of $k_{\text{peak}}[|\nabla \times \omega|^2](t)$ terminates in a short plateau near its maximum.

For visualization and as auxiliary reference values in the Q -snapshot figures (Figs. 1–5), we also report reaching times for more global metrics such as k_{centroid} and k_{95} . For a generic k -metric $k_m(t)$, we define $k_m^\varepsilon \equiv k_m(t_\varepsilon)$ and, for a threshold $q \in (0, 1)$,

$$t_{m,q} \equiv \min \{t : k_m(t') \geq q k_m^\varepsilon \ \forall t' \in [t, t + M \Delta t_{\text{out}}]\}, \quad (41)$$

where Δt_{out} is the output interval and we take $M = 3$. In the snapshots we denote $t_c \equiv t_{k_{\text{centroid}}[|\nabla \times \omega|^2], q}$ and $t_{95} \equiv t_{k_{95}[|\nabla \times \omega|^2], q}$ with $q = 0.9$. Because the reaching-time criterion depends on the choice of (q, M) , we use t_c and t_{95} only as auxiliary markers and do not rely on them for the primary ordering arguments.

All characteristic times reported in this work are extracted from time series sampled at the output cadence $\Delta t_{\text{out}} = 5 \times 10^{-2}$ (Sec. III B). Therefore, t_k , t_ε , and t_Π are quantized in steps of Δt_{out} and carry an intrinsic temporal discretization uncertainty of $\mathcal{O}(\Delta t_{\text{out}})$. Conservatively, we take $|\delta t_k|, |\delta t_\varepsilon|, |\delta t_\Pi| \leq \Delta t_{\text{out}}$, which implies $|\delta \Delta t_{k_\varepsilon}|, |\delta \Delta t_{\varepsilon \Pi}| \leq 2 \Delta t_{\text{out}}$ for the lead/lag measures. In all cases summarized in Table I, the observed separations exceed this bound; in particular, the smallest lead time $\Delta t_{k_\varepsilon} = 0.40$ corresponds to $8 \Delta t_{\text{out}}$, so the ordering is robust to the output cadence.

In all cases of Figs. 9–14, t_k consistently precedes t_ε , while t_Π occurs later than t_ε , establishing the ordering $t_k < t_\varepsilon < t_\Pi$ across the tested initial conditions. The centroid- and quantile-type measures (k_{centroid} and k_{95}) exhibit the same qualitative behavior, providing an additional robustness check beyond a single peak definition.

F. Inspection for high- k locking and cutoff effects

Because $|\nabla \times \omega|^2(k)$ involves a strong k^4 weighting, peak-based indicators can be particularly sensitive to finite-resolution effects in the high- k range. In extreme transient states, this sensitivity may lead to spurious

peak detection if the argmax is influenced by spectral content close to the analysis cutoff. To assess this possibility, we explicitly inspect $|\nabla \times \omega|^2(k)$ at representative times and mark the detected peak locations, as summarized in Fig. 8.

For the 512^3 ABC-based cases and the TGV at the baseline viscosity $\nu = 10^{-3}$, the spectrum exhibits a clear maximum of $|\nabla \times \omega|^2(k)$ that is well separated from the cutoff. In contrast, for the Kida–Pelz case at 512^3 , the instantaneous argmax can approach $k_{\max}^{(\text{mask})}$ during the early transient, indicating a cutoff-proximate “locking” of the peak. This behavior is visualized explicitly in Fig. 8(e) and reflects the combination of intense small-scale generation in the Kida–Pelz flow and the strong high- k bias inherent in the k^4 weighting.

In this work we treat cutoff-proximate peaks as a *resolution warning* rather than as a feature to be “corrected” by an alternative peak definition. This inspection protocol is applied throughout the paper to all simulations reported here, including the viscosity-variation TGV runs in Sec. V F. When cutoff-proximate locking is encountered (as in the 512^3 Kida–Pelz case and the low-viscosity TGV case), we do not attempt to suppress it by an ad hoc restriction of the peak-search interval; instead, we treat it as a resolution warning and rely on a higher-resolution companion simulation for quantitative comparison.

Accordingly, to verify that the near-cutoff peak locking observed in the 512^3 Kida–Pelz run is not physical, we performed a companion simulation at 1024^3 . As shown in Fig. 8(f), the higher-resolution spectrum exhibits a well-defined peak away from the cutoff and shows no tendency toward high- k locking. This confirms that the issue observed at 512^3 originates from limited resolution rather than from the underlying dynamics.

Based on this assessment, the Kida–Pelz results discussed in the remainder of this paper are taken from the 1024^3 simulation, while the 512^3 case is retained solely to demonstrate the resolution sensitivity of peak detection in curvature-weighted spectra.

V. RESULTS

A. Resolution diagnostics and Reynolds-number evolution

We begin by confirming that all runs are adequately resolved over the time intervals analyzed. Figure 6 shows the time series of the Taylor-scale Reynolds number $R_\lambda(t)$ together with the resolution indicator $k_{\max}\eta(t)$, where $k_{\max} = (N/2)2\pi/L$ is the Nyquist wavenumber (as in Ref. [9]) and $\eta(t) = (\nu^3/\varepsilon(t))^{1/4}$ is the Kolmogorov length. For all 512^3 cases (Multi-ABC, Multi-ABC asymmetric, ABC+random-phase low- k , TGV, and Kida–Pelz), $k_{\max}\eta(t)$ remains above unity throughout the evolution, including around the dissipation episode, indicating that the smallest dynamically relevant scales are captured. The concomitant decrease of $R_\lambda(t)$ during the

dissipation surge reflects the rapid development of small scales and the accompanying increase of the characteristic gradients.

For the Kida–Pelz initial condition, we additionally performed a 1024^3 simulation (shown as the high-resolution counterpart in Fig. 6) to address a peak-detection issue in the curvature-weighted spectrum (discussed below). As expected, the higher-resolution run provides a substantially larger $k_{\max}\eta(t)$ margin over the entire time interval, which helps disentangle physical peak motion from finite-resolution artifacts.

B. Evolution of integral and dissipative scales

Figure 7 summarizes the evolution of representative scale measures $L_{\text{int}}(t)$, the Taylor microscale $\lambda(t)$, the Kolmogorov scale $\eta(t)$, and the dissipation rate $\varepsilon(t)$ for all cases. Across initial conditions, the same qualitative pattern is observed: as the flow transitions from its initially organized large-scale state toward a turbulent, volume-filling state, the energy-containing scale L_{int} and the intermediate scale λ decrease, while η decreases toward its minimum near the dissipation peak and then increases during late-time decay.

The principal difference across cases is the characteristic time window over which this transient unfolds. The structured ABC-based initial conditions (Multi-ABC and its asymmetric variant) exhibit a comparatively rapid onset of small-scale activity followed by a long decay, whereas the ABC+random-phase low- k case develops and dissipates more slowly, consistent with the prolonged persistence of large-scale organization seen in the Q -criterion snapshots (Sec. III). The TGV evolution reproduces the canonical timescale separation reported previously [9], while the Kida–Pelz flow produces strong gradients very rapidly, in line with the known propensity of this highly symmetric configuration to generate intense small-scale structures [12, 13].

These scale trends provide an important backdrop for interpreting curvature-weighted spectral indicators: the precursor times identified below consistently occur during the phase in which $\eta(t)$ is still decreasing and the flow morphology is transitioning toward filament/tube-dominated structures.

C. Spike inspection for the curvature-weighted spectrum

A central observable in this work is the curvature-weighted spectrum $|\nabla \times \omega|^2(k)$ (equivalently $k^4 E(k)$ for incompressible flow), and the associated peak/centroid/quantile wavenumber measures introduced in Sec. IV. Because $|\nabla \times \omega|^2(k)$ strongly emphasizes high wavenumbers, its instantaneous argmax can be particularly sensitive to finite-resolution effects near the analysis cutoff $k_{\max}^{(\text{mask})}$. Following the inspection

protocol described in Sec. IV F, we therefore perform an explicit *spike inspection*: we examine representative spectra and verify whether the detected maximizer lies well inside the resolved range. If the maximizer lies at (or very close to) $k_{\max}^{(\text{mask})}$, we interpret this as a *resolution warning* and rely on a higher-resolution companion simulation for quantitative extraction of characteristic times. Importantly, we do *not* remove, trim, or otherwise exclude peaks; the inspection is used only to flag cutoff-proximate peak locking.

Figure 8 presents representative inspections of $|\nabla \times \omega|^2(k)$ at selected times, with the detected peak marked. For the Multi-ABC, Multi-ABC (Asymmetric), ABC+random-phase low- k , and TGV cases, the spectrum exhibits a well-defined maximum at intermediate-to-small scales at the inspected time, and the peak is clearly separated from $k_{\max}^{(\text{mask})}$ (the spherical two-thirds cutoff). In contrast, for the Kida–Pelz case at 512^3 , the maximizer can approach $k_{\max}^{(\text{mask})}$ during the early transient, indicating cutoff-proximate peak locking [Fig. 8(e)]. This endpoint hit is also visible in the time-series view in Fig. 13, where $k_{\text{peak}}[|\nabla \times \omega|^2](t)$ can reach $k_{\max}^{(\text{mask})}$. Accordingly, we use the 1024^3 Kida–Pelz data (Figs. 8(f) and 14) as the reference for the Kida–Pelz precursor analysis, while retaining the 512^3 case only to illustrate this finite-resolution failure mode.

D. Precursor behavior and robust temporal ordering across initial conditions

We now present the main comparative results. Figures 9–14 show the time evolution of the characteristic wavenumber measures derived from the curvature-weighted spectrum $|\nabla \times \omega|^2(k)$ together with the dissipation rate $\varepsilon(t)$ (and, in the corresponding flux panels, the characteristic measures derived from $|\Pi(K, t)|$). The vertical markers indicate the characteristic times defined in Sec. IV: t_k for the curvature-weighted precursor, t_ε for the dissipation peak, and t_Π for the largest-flux-peak scale time.

Across all cases, the precursor time associated with the curvature-weighted spectrum occurs first:

$$t_k < t_\varepsilon, \quad (42)$$

and the flux-related time occurs last,

$$t_\varepsilon < t_\Pi, \quad (43)$$

thereby establishing the robust ordering

$$t_k < t_\varepsilon < t_\Pi \quad (44)$$

beyond the TGV setting of Ref. [9]. Importantly, this conclusion does not rely on a single, potentially noisy definition of a “peak”. Figures 9–14 show that alternative wavenumber characterizations—including centroid-type and quantile-type measures (e.g., k_c and k_{95} , and

their associated characteristic times)—exhibit the same qualitative advance relative to t_ε , providing evidence that the precursor is a robust feature of the overall spectral redistribution rather than a fragile local maximizer.

The comparative view also clarifies how initial-condition-dependent transients modulate the magnitude of the lead time while preserving the ordering. In the ABC+random-phase low- k case, the entire evolution is stretched, and both t_k and t_ε occur later than in the structured ABC-based cases; nevertheless, the curvature-weighted measures still rise and stabilize before the dissipation maximum. In the Kida–Pelz configuration, the precursor develops extremely early, consistent with the rapid formation of tightly curved tubes and sheets seen in the Q -criterion visualizations (Sec. III), and the high-resolution run confirms that this early stabilization is a physical feature rather than an artifact of insufficient small-scale resolution.

Finally, the flux-based characteristic measures evolve more slowly than their curvature-weighted counterparts, reflecting the fact that $|\Pi|$ is an integral indicator of net interscale transfer and therefore lags the initial formation of high-curvature structures that viscosity will soon act upon. This systematic lag underlies the observed ordering $t_\varepsilon < t_\Pi$ across all cases.

E. Summary of characteristic times

Table I summarizes, for each initial condition, the characteristic times t_k , t_ε , and t_Π extracted from the peak-time definitions introduced in Sec. IV, together with the corresponding lead and lag times,

$$\Delta t_{k\varepsilon} \equiv t_\varepsilon - t_k, \quad \Delta t_{\varepsilon\Pi} \equiv t_\Pi - t_\varepsilon. \quad (45)$$

The table makes the cross-case robustness of the temporal ordering

$$t_k < t_\varepsilon < t_\Pi \quad (46)$$

immediately apparent, while also quantifying how the lead and lag magnitudes vary with the initial condition.

In particular, $\Delta t_{k\varepsilon}$ provides a compact measure of how far in advance the curvature-weighted diagnostic stabilizes relative to the dissipation peak, whereas $\Delta t_{\varepsilon\Pi}$ quantifies the systematic delay of the flux-related characteristic time. Across all cases listed in Table I, the precursor time t_k consistently precedes t_ε , and the flux-related time t_Π occurs later, demonstrating that the ordering $t_k < t_\varepsilon < t_\Pi$ is not restricted to a single initial condition.

For the Kida–Pelz flow, only the 1024^3 results are reported in Table I. As discussed in Sec. IV F, the 512^3 simulation can exhibit cutoff-proximate peak locking in the k^4 -weighted spectrum during the early transient, whereas the higher-resolution run provides a well-resolved peak away from the cutoff and a reliable basis for extracting characteristic times. The 512^3 Kida–Pelz case is therefore excluded from the summary table and is used only

to illustrate resolution sensitivity and diagnostic considerations.

Additional robustness information based on alternative wavenumber measures, including centroid- and quantile-type definitions (e.g., k_{centroid} and k_{95} for both $|\nabla \times \omega|^2$ and $|\Pi|$), is provided in all cases of Figs. 9–14 and supports the same qualitative temporal ordering.

For visualization in the Q-snapshot sequences (Figs. 1–5), we annotated auxiliary reaching times t_c and t_{95} based on global measures of the curvature-weighted spectrum (k_{centroid} and k_{95}), using the sustained-threshold definition in Eq. (41) (with $q = 0.9$ and $M = 3$). Because Eq. (41) is defined relative to $k_m^\epsilon \equiv k_m(t_\epsilon)$, these reaching times are *retrospective* by construction and were not used in the primary ordering arguments. Nevertheless, the relative timing of (t_c, t_{95}) with respect to t_ϵ provides a compact diagnostic of whether bulk redistribution toward small scales approaches its t_ϵ -level appreciably before, or only near, the dissipation peak. Table II summarizes the annotated values from Figs. 1–5. For the Kida–Pelz case, although Fig. 5 shows the 512^3 visualization, we verified that the measured values of t_ϵ , t_c , and t_{95} are identical in the companion 1024^3 reference simulation used elsewhere for the Kida–Pelz analysis (Sec. IV F and Table I), so the values are representative of the resolved Kida–Pelz dynamics.

F. Viscosity dependence in Taylor–Green turbulence

The ordering $t_k < t_\epsilon < t_\Pi$ established above pertains to the baseline viscosity $\nu = 10^{-3}$. To examine how this temporal ordering depends on the viscous damping of small scales, we repeat the TGV simulations at two additional viscosities, $\nu = 2.5 \times 10^{-4}$ and $\nu = 10^{-2}$, while keeping the numerical scheme and the post-processing pipeline unchanged.

Figure 15 shows the low-viscosity case $\nu = 2.5 \times 10^{-4}$. At 512^3 , we observed (not shown) that the intensified small-scale activity, together with the k^4 weighting in $|\nabla \times \omega|^2(k)$, drives the instantaneous argmax toward the analysis cutoff, leading to cutoff-proximate peak “locking” (cf. the baseline Kida–Pelz behavior discussed in Sec. IV F). We therefore treat the 512^3 low-viscosity run as under-resolved for peak detection and use a 1024^3 simulation as the reference for this case. The spectrum inspection in Fig. 16(c) confirms that the detected peak of $|\nabla \times \omega|^2(k)$ is well separated from the cutoff at representative times. With this adequately resolved dataset, the argmax-based peak scales again satisfy $t_k < t_\epsilon < t_\Pi$.

In contrast, the high-viscosity case $\nu = 10^{-2}$ (Fig. 17) shows that the temporal ordering can change in a more strongly viscous, lower-Reynolds-number decay. Here the spectrum remains comfortably separated from the cutoff (Fig. 18(c)) and the resolution indicator $k_{\max} \eta$ stays large (Fig. 18(a)), so the change in ordering is not attributable to high- k locking. Instead, the dissipation peak occurs

earlier than the time at which the curvature-weighted peak scale reaches its maximum, i.e. $t_\epsilon < t_k$ (and t_Π becomes comparable to t_k).

This breakdown is physically natural because the curvature-weighted spectrum is dominated by the highest resolved wavenumbers and is therefore strongly affected by viscous damping. In Fourier space the energy spectrum obeys

$$\partial_t E(k, t) = T(k, t) - 2\nu k^2 E(k, t), \quad (47)$$

so the curvature-weighted quantity $C(k, t) \equiv k^4 E(k, t)$ satisfies

$$\partial_t C(k, t) = k^4 T(k, t) - 2\nu k^2 C(k, t), \quad (48)$$

which shows that increasing ν accelerates the decay of high- k contributions at a rate $\propto \nu k^2$. Consequently, when viscosity is large enough that the dissipative term dominates the high- k balance, the early advance of the peak scale observed at lower viscosity is weakened or can even reverse, reducing (or changing the sign of) the lead time Δt_{k_ϵ} .

These two additional TGV runs therefore indicate that the ordering $t_k < t_\epsilon < t_\Pi$ is robust across moderate-to-low viscosities but is not universal once viscous effects dominate the small-scale spectrum.

VI. DISCUSSION

A. Physical interpretation of the ordering

$$t_k < t_\epsilon < t_\Pi$$

The central finding of this study is that, for a broad class of freely decaying flows at moderate-to-low viscosity (including all baseline cases at $\nu = 10^{-3}$ and the low-viscosity TGV run at $\nu = 2.5 \times 10^{-4}$), the time t_k at which the peak scale of the curvature-weighted spectrum $|\nabla \times \omega|^2(k) = k^4 E(k)$ attains its maximum precedes the dissipation peak time t_ϵ , and t_ϵ precedes the flux-related characteristic time t_Π , i.e., $t_k < t_\epsilon < t_\Pi$. The additional high-viscosity TGV run at $\nu = 10^{-2}$ (Sec. V F) provides a counterexample in which $t_\epsilon < t_k$, highlighting that the ordering is a high-Reynolds-number feature rather than a kinematic identity.

Here we discuss a physical interpretation of this ordering in the context of non-stationary cascade development.

First, $|\nabla \times \omega|^2(k)$ is a curvature-biased measure: in incompressible flow $\nabla \times \omega = -\nabla^2 \mathbf{u}$, and therefore $|\nabla \times \omega|^2(k) = k^4 E(k)$ strongly emphasizes the emergence of high-wavenumber content. The advance of its characteristic wavenumber measures thus reflects the *reach* of the flow toward small scales in wavenumber space. In a transient, freely decaying setting, the appearance of small scales in this sense can occur early, driven by vortex stretching and folding and by the rapid steepening of gradients in localized regions.

However, the dissipation rate $\varepsilon(t) = 2\nu \sum_k k^2 E(k, t)$ does not depend only on the *reach* in k but also on how much energy has accumulated in the dissipative range. Even after the k^4 -weighted spectrum has developed a stable peak scale, the dissipative-range energy content can continue to grow for some time, leading naturally to a later maximum of $\varepsilon(t)$. This provides a mechanistic rationale for why $t_k < t_\varepsilon$ is expected in non-stationary transients.

Finally, the flux-based characteristic time t_Π is extracted from $|\Pi(K)|$, which is an integrated measure of net transfer across a scale. Compared with $|\nabla \times \boldsymbol{\omega}|^2(k)$, the flux diagnostic is less localized in k and reflects the organization of triadic interactions across a range of scales [1, 2]. In a decaying transient, it is therefore plausible that the small-scale reach and the subsequent dissipation surge precede the time at which the flux-related peak scale $k_{\text{peak}}[\Pi](t)$ attains its maximum. In this view, $t_\varepsilon < t_\Pi$ reflects that the dissipation maximum can occur while the cascade is still evolving toward its most pronounced interscale-transfer configuration.

B. Initial-condition robustness and what varies across cases

A key motivation for the present work was to determine whether the precursor reported for TGV is tied to its special symmetries or instead reflects a more general feature of small-scale formation in 3D turbulence. Figures 9–14 evidently show that the temporal ordering persists for (i) structured helical ABC-based flows, (ii) a symmetry-broken multi-mode ABC superposition, (iii) an ABC flow with additional random-phase low- k content, and (iv) the high-symmetry Kida–Pelz configuration [12, 13]. This strongly suggests that the precursor is not specific to a particular topology or symmetry class.

While the ordering is robust, the *timescales* vary substantially. This is consistent with the fact that the route from initial organization to volume-filling turbulence depends on the initial distribution of energy across large scales and on how quickly strong gradients develop. For example, the ABC+random-phase low- k case exhibits a stretched evolution in which both t_k and t_ε occur later than in the purely structured ABC-based cases, whereas the Kida–Pelz flow produces strong gradients very rapidly. Such differences are also apparent in the evolution of global scales (Fig. 7) and in the Q -criterion visualizations (Sec. III), which qualitatively indicate when tube-/sheet-dominated morphology becomes prevalent.

In this sense, t_k acts as an *early warning* marker whose absolute value is initial-condition dependent, but whose relative position with respect to t_ε and t_Π appears to be a generic feature within the parameter range studied here (fixed ν , periodic box, freely decaying evolution).

C. Why $k^4 E(k)$ is a sensitive precursor and why spike inspection is essential

The attractiveness of the curl-of-vorticity spectrum as a precursor lies in the strong k^4 weighting, which amplifies the incipient development of small-scale content and makes the advance of a characteristic wavenumber conspicuous already in the early transient. This sensitivity is precisely what allows t_k to precede t_ε in all cases examined.

At the same time, the same strong weighting makes peak-based metrics potentially vulnerable to finite-resolution effects near the spectral cutoff. A near-cutoff “spike” can arise from a combination of limited scale separation, discretization noise, and the rapid growth of high- k tails during intense transients. Figure 8 illustrates this issue most clearly for the Kida–Pelz initial condition at 512^3 , where the naive argmax of $|\nabla \times \boldsymbol{\omega}|^2(k)$ can approach the largest resolved wavenumbers.

This motivates explicit spike inspection (Sec. IV F), together with a resolution check using $k_{\text{max}}\eta(t)$ (Fig. 6) and a higher-resolution reference for Kida–Pelz. In this paper we do not “correct” peak locations by excluding a near-cutoff band; instead, cutoff-proximate peaks are used solely as a resolution diagnostic and motivate higher-resolution reference simulations. In practice, the combination of (i) monitoring $k_{\text{max}}\eta$, (ii) inspecting $|\nabla \times \boldsymbol{\omega}|^2(k)$ at representative times, and (iii) comparing peak-based measures with more global k -metrics such as k_{centroid} and k_{95} , provides a robust workflow for deploying curvature-weighted diagnostics without conflating physical peak motion with cutoff artifacts.

An important practical implication is that spike inspection, while not standard for lower-order spectral measures, is a natural and necessary component of analyses based on k^4 -weighted spectra. Including this check (Fig. 8) strengthens the credibility of the precursor claim, particularly when comparing different initial conditions whose transient intensities differ markedly.

D. Physical meaning of the curvature-weighted diagnostic.

In incompressible flow, $\nabla \cdot \mathbf{u} = 0$ implies $\nabla \times \boldsymbol{\omega} = -\nabla^2 \mathbf{u}$, so the spectrum $|\nabla \times \boldsymbol{\omega}|^2(k, t)$ emphasized in this work is equivalently a spectral density of the Laplacian of the velocity (Sec. II C and Eq. (30)). While this may suggest a purely “diffusive” interpretation, it is useful to recall that the *integral* of this quantity has a standard meaning in turbulence theory. Indeed, the volume integral of $|\nabla \times \boldsymbol{\omega}|^2$ coincides (up to conventional factors) with the *palinstrophy*,

$$\mathcal{P}(t) \equiv \frac{1}{2} \langle |\nabla \boldsymbol{\omega}|^2 \rangle = \frac{1}{2} \langle |\nabla \times \boldsymbol{\omega}|^2 \rangle, \quad (49)$$

whose isotropic spectral density is precisely $k^4 E(k, t)$ (with our spectral normalization). Palinstrophy enters

directly as the viscous sink of enstrophy in the enstrophy budget,

$$\frac{d}{dt} \left(\frac{1}{2} \langle |\boldsymbol{\omega}|^2 \rangle \right) = \langle \boldsymbol{\omega} \cdot \mathbf{S} \cdot \boldsymbol{\omega} \rangle - \nu \langle |\nabla \boldsymbol{\omega}|^2 \rangle, \quad (50)$$

where $\mathbf{S} = (\nabla \mathbf{u} + \nabla \mathbf{u}^\top)/2$ is the strain-rate tensor. Since for periodic incompressible flow $\varepsilon(t) = \nu \langle |\nabla \mathbf{u}|^2 \rangle = \nu \langle |\boldsymbol{\omega}|^2 \rangle$, Eq. (50) implies that palinstrophy controls (through the viscous term) the rate at which enstrophy—and therefore dissipation—can turn over. From this viewpoint, the observed “advance and saturation” of a characteristic wavenumber of $|\nabla \times \boldsymbol{\omega}|^2(k, t)$ provides an early indicator that vorticity gradients have reached their dynamically active range in k -space, *before* sufficient energy has accumulated in the dissipative band to maximize $\varepsilon(t)$. Importantly, this interpretation does not imply that diffusion *creates* small scales; rather, nonlinear stretching/folding creates steep gradients, and the curvature-weighted measure identifies where viscous action will soon become dominant.

On the role of $\nabla \times \boldsymbol{\omega}$ beyond classical Newtonian continua. The quantity $\nabla \times \boldsymbol{\omega}$ is also discussed in several applied contexts under different names and modeling frameworks. In generalized continuum theories that allow additional rotational degrees of freedom or couple stresses, terms proportional to $\nabla \times \boldsymbol{\omega}$ can appear explicitly as constitutive (dissipative) contributions, often described as a “rotational viscosity” or related couple-stress mechanism (e.g., micropolar fluid theory [19–22]). We do not attempt to take a position on the long-standing debate regarding the physical status of such generalized continuum descriptions for ordinary fluids; accordingly, we adopt the neutral term *curvature-weighted* to emphasize the mathematical role of the k^4 weighting in classical incompressible Navier–Stokes turbulence. Nevertheless, the robustness of the precursor behavior reported here suggests that $\nabla \times \boldsymbol{\omega}$ -based diagnostics can, under certain conditions, act as a sensitive marker of impending small-scale activity and dissipation surges. Clarifying how (and whether) similar precursor behavior manifests in generalized continuum models, and how it connects to practical “online” monitoring strategies, is an interesting direction for future work.

E. Relation to transient cascade development and dissipation dynamics

The present observations are consistent with a general picture of transient cascade development in decaying turbulence. The early advance of the curvature-weighted spectral peak indicates that the flow reaches small scales in wavenumber space rapidly, which aligns with the emergence of tightly curved tubes and rolled-up sheets visible in the Q -criterion snapshots (Sec. III). The subsequent dissipation peak reflects the accumulation of sufficient energy at dissipative scales, and the later flux-related

characteristic time reflects the continued evolution of interscale transfer organization.

From this perspective, the ordering $t_k < t_\varepsilon < t_\Pi$ can be interpreted as a temporal separation between (i) the formation of small-scale *reach* (geometry/curvature), (ii) the maximum of viscous activity (dissipation), and (iii) the maturation of the most prominent transfer configuration captured by $|\Pi|$. This separation is expected to be most visible in non-stationary transients where the cascade is not in equilibrium. The fact that the ordering persists across initial conditions suggests that it is linked to generic properties of the nonlinear term and to how gradients build up before they are fully dissipated.

F. Limitations and outlook

The present study focuses on freely decaying turbulence in a periodic box at fixed viscosity $\nu = 10^{-3}$, with a base resolution of 512^3 and an additional 1024^3 reference for Kida–Pelz. While this setup allows a controlled comparison across initial conditions, several extensions would be valuable.

First, it remains to quantify how the lead time $\Delta t_{k_\varepsilon} = t_\varepsilon - t_k$ depends on Reynolds number and viscosity. Second, it would be important to test whether analogous precursor behavior persists in statistically stationary forced turbulence, where the balance between injection, transfer, and dissipation differs from the freely decaying case. Third, extensions to flows with stronger anisotropy or additional physics (e.g., rotation, stratification, magnetohydrodynamics) would clarify the domain of applicability of curvature-weighted precursors.

From a practical viewpoint, the precursor is most interesting in online or near-real-time settings. The argmax-based definitions of t_k and t_Π used in this paper are inherently retrospective because they require the future evolution to identify a global maximum. For online monitoring one could instead track a running maximum of $k_{\text{peak}}[|\nabla \times \boldsymbol{\omega}|^2](t)$ (and/or its growth rate) and trigger an “alert time” when the running maximum saturates (plateau detection) or when k_{peak} exceeds a prescribed threshold calibrated from reference datasets. A systematic evaluation of such online variants—including sensitivity to output cadence and the cutoff-spike inspection discussed in Sec. IV F—is left for future work.

Toward operational (online) early warning: an edge-bulk hybrid trigger. Table II shows that reaching-time markers based on global k -metrics can provide an appreciable lead relative to the dissipation peak for several initial conditions (including the Kida–Pelz case, for which t_ε , t_c , and t_{95} were confirmed to be identical in the 1024^3 reference run), but may be near-concurrent with, or even lag, t_ε in others. This case dependence is consistent with the fact that centroid/quantile measures reflect bulk redistribution and can be sensitive to non-monotonic adjustments when a sustained-threshold (“hold”) requirement is imposed (Eq. (41)). For operational monitoring,

TABLE I. Summary of characteristic times for all initial conditions. Definitions follow Sec. IV. All characteristic times are extracted on the output-time grid with spacing $\Delta t_{\text{out}} = 5 \times 10^{-2}$, implying a sampling uncertainty of $\pm \Delta t_{\text{out}}/2$ for each time and $\mathcal{O}(\pm \Delta t_{\text{out}})$ for the lead/lag measures.

Case	N^3	t_k	t_ϵ	t_Π	$\Delta t_{k\epsilon}$	$\Delta t_{\epsilon\Pi}$
Multi-ABC	512^3	22.60	26.60	28.95	4.00	2.35
Multi-ABC (Asymmetric)	512^3	27.00	30.00	53.75	3.00	23.75
ABC + random-phase low- k	512^3	48.95	51.30	68.45	2.35	17.15
TGV	512^3	6.55	9.00	11.20	2.45	2.20
Kida–Pelz (high resolution)	1024^3	3.00	3.40	7.15	0.40	3.75

TABLE II. Auxiliary reaching-time markers t_c and t_{95} (Eq. (41), with $q = 0.9$ and $M = 3$) annotated in the Q-snapshot figures, and their lead/lag relative to the dissipation-peak time t_ϵ . We report $\Delta t_{ce} \equiv t_\epsilon - t_c$ and $\Delta t_{95\epsilon} \equiv t_\epsilon - t_{95}$ (positive values indicate *lead* relative to t_ϵ). Because all times are sampled on the output-time grid with spacing $\Delta t_{\text{out}} = 5 \times 10^{-2}$, differences with $|\Delta t| \leq 2\Delta t_{\text{out}} = 0.1$ should be regarded as near-concurrent at the present cadence (cf. Sec. IV E). For Kida–Pelz, the Q-snapshot annotations are taken from Fig. 5 (512^3 visualization), but the same values (t_ϵ , t_c , and t_{95}) were confirmed in the companion 1024^3 reference run (Sec. IV F), and thus can be interpreted on equal footing with the other cases. The peak-based characteristic-time summary in Table I still uses the 1024^3 Kida–Pelz reference dataset, consistent with our resolution-inspection protocol.

Case	t_ϵ	t_c	t_{95}	Δt_{ce}	$\Delta t_{95\epsilon}$	Note
Multi-ABC	26.60	27.00	26.85	-0.40	-0.25	lag (fails)
Multi-ABC (Asymmetric)	30.00	25.90	25.90	4.10	4.10	lead (succeeds)
ABC + random-phase low- k	51.30	50.15	49.60	1.15	1.70	lead (succeeds)
TGV	9.00	9.15	9.05	-0.15	-0.05	near-concurrent at this cadence
Kida–Pelz	3.40	2.20	2.20	1.20	1.20	lead (succeeds; confirmed at 1024^3)

it is therefore natural to treat global metrics primarily as *confirmatory* or *robustness* indicators, while using a leading-edge-sensitive diagnostic to provide the earliest alert.

To make this idea concrete on the discrete output grid $t_n = n\Delta t_{\text{out}}$, define $k_p(t_n) \equiv k_{\text{peak}}[|\nabla \times \boldsymbol{\omega}|^2](t_n)$ and the running maximum

$$k_p^{\max}(t_n) \equiv \max_{0 \leq m \leq n} k_p(t_m). \quad (51)$$

An online analogue of the “advance-and-saturation” notion is the first time at which the running maximum has not increased over the past M outputs:

$$t_{\text{sat}}^{(p)} \equiv \min \{t_n : k_p^{\max}(t_n) = k_p^{\max}(t_{n-M})\}, \quad (52)$$

which can be evaluated sequentially with a detection latency of $M\Delta t_{\text{out}}$. To reduce false alarms (e.g. cutoff-proximate peak locking), one may combine this edge trigger with a bulk confirmation based on the centroid growth rate,

$$g_c(t_n) \equiv \frac{k_{\text{centroid}}[|\nabla \times \boldsymbol{\omega}|^2](t_n) - k_{\text{centroid}}[|\nabla \times \boldsymbol{\omega}|^2](t_{n-M})}{M\Delta t_{\text{out}}}, \quad (53)$$

and a simple cutoff-proximity guard,

$$\mathcal{L}(t_n) \equiv \mathbf{1} \left[k_p(t_n) \geq \chi k_{\text{max}}^{\text{mask}} \right], \quad (54)$$

where $k_{\text{max}}^{\text{mask}}$ is defined in Eq. (24) and $\chi \in (0, 1)$ (e.g. $\chi = 0.9$) sets a conservative margin. A minimal hybrid alert time can then be defined as

$$t_{\text{alert}} \equiv \min \left\{ t_n \geq t_{\text{sat}}^{(p)} : g_c(t_n) \geq g_{c,\text{th}} \wedge \mathcal{L}(t_n) = 0 \right\}, \quad (55)$$

with a tunable threshold $g_{c,\text{th}}$. Systematically evaluating such online variants—including sensitivity to $(M, \chi, g_{c,\text{th}})$ and to the output cadence Δt_{out} , and benchmarking across initial conditions and viscosity—is an important direction for future work.

VII. CONCLUSIONS

We investigated spectral precursors to the dissipation peak in freely decaying, three-dimensional turbulence by extending our recent PRF Letter on the Taylor–Green vortex (TGV) [9] to a broader set of initial conditions. Using pseudo-spectral direct numerical simulations in a 2π -periodic box at $\nu = 10^{-3}$, we considered five distinct 512^3 runs (Multi-ABC, asymmetric Multi-ABC, ABC with random-phase low- k perturbations, TGV, and Kida–Pelz) and an additional 1024^3 reference run for Kida–Pelz. All data were analyzed using a unified post-processing pipeline for isotropic spectra, transfer, and flux diagnostics.

Our main conclusion is that the characteristic time

associated with the advance of the curvature-weighted diagnostic $|\nabla \times \omega|^2(k) = k^4 E(k)$ robustly precedes the dissipation peak time, and that the dissipation peak precedes the flux-related characteristic time extracted from $|\Pi(K)|$. Across all tested initial conditions we consistently observe the temporal ordering

$$t_k < t_\varepsilon < t_{\Pi}, \quad (56)$$

thereby demonstrating that the precursor behavior reported previously for TGV is not restricted to that highly symmetric benchmark. Moreover, alternative wavenumber measures based on centroid and quantile definitions (e.g., k_{centroid} and k_{95}) exhibit the same qualitative early-warning behavior, supporting the robustness of the precursor beyond a single peak-based metric.

A notable methodological outcome is that curvature-weighted spectra require explicit spike inspection for cutoff-proximate artifacts. Because $|\nabla \times \omega|^2(k)$ strongly emphasizes high wavenumbers, naive peak extraction can be contaminated when the argmax is influenced by near-cutoff behavior, as illustrated for the 512^3 Kida–Pelz case. We therefore combined (i) resolution diagnostics using $k_{\max} \eta(t)$, (ii) direct inspections of $|\nabla \times \omega|^2(k)$, and (iii) higher-resolution reference simulations where required (Kida–Pelz and the low-viscosity TGV case). These procedures ensure that the extracted characteristic times reflect genuine small-scale dynamics rather than

finite-resolution locking.

The results presented here suggest that curvature-weighted spectral diagnostics provide a practical and broadly applicable early indicator of impending dissipation activity in non-stationary turbulent transients. In addition to their conceptual value for understanding transient cascade development, these diagnostics may enable operational uses in large-scale simulations, such as scheduling dense output around the dissipation episode or triggering adaptive resolution strategies.

Several directions remain open. The viscosity-variation TGV runs in Sec. V F provide a first indication of Reynolds-number (viscosity) dependence: the ordering persists at lower viscosity but can break at higher viscosity, where viscous damping suppresses the early-time advance of the curvature-weighted peak scale. A systematic map of the lead time $\Delta t_{k\varepsilon} = t_\varepsilon - t_k$ versus Reynolds number, viscosity, and initial spectral content remains an important direction, as does testing the precursor in statistically stationary forced turbulence and exploring extensions to anisotropic or multi-physics settings. These studies will help delineate the generality and practical scope of curvature-weighted precursors in turbulent flows.

Acknowledgments. This study was supported by JSPS KAKENHI (Grant Number 22K14177) and JST PRESTO (Grant Number JPMJPR23O7).

[1] U. Frisch, *Turbulence: The Legacy of A. N. Kolmogorov* (Cambridge University Press, Cambridge, 1995).

[2] A. Alexakis and L. Biferale, Cascades and transitions in turbulent flows, *Physics Reports* **767-769**, 1 (2018).

[3] M. E. Brachet, D. Meiron, S. Orszag, B. Nickel, R. Morf, and U. Frisch, The taylor-green vortex and fully developed turbulence, *Journal of Statistical Physics* **34**, 1049 (1984).

[4] J. R. DeBonis, *Solutions of the Taylor–Green Vortex Problem Using High-Resolution Explicit Finite Difference Methods*, NASA Technical Memorandum NASA/TM-2013-217850 (NASA Glenn Research Center, Cleveland, Ohio, 2013) NASA Technical Memorandum.

[5] J. I. Cardesa, A. Vela-Martín, S. Dong, and J. Jiménez, The temporal evolution of the energy flux across scales in homogeneous turbulence, *Physics of Fluids* **27**, 111702 (2015).

[6] P. C. Valente, R. Onishi, and C. B. da Silva, Origin of the imbalance between energy cascade and dissipation in turbulence, *Physical Review E* **90**, 023003 (2014).

[7] J. C. R. Hunt, A. A. Wray, and P. Moin, Eddies, streams, and convergence zones in turbulent flows, in *Studying Turbulence Using Numerical Simulation Databases*, 2 (NASA, Washington, DC, 1988) pp. 193–208.

[8] M. S. Chong, A. E. Perry, and B. J. Cantwell, A general classification of three-dimensional flow fields, *Physics of Fluids A: Fluid Dynamics* **2**, 765 (1990).

[9] S. Tsuzuki, Spectrum of the curl of vorticity as a precursor to dissipation in three-dimensional taylor-green turbulence, *Phys. Rev. Fluids* **11**, L012601 (2026).

[10] G. I. Taylor and A. E. Green, Mechanism of the production of small eddies from large ones, *Proceedings of the Royal Society of London. Series A - Mathematical and Physical Sciences* **158**, 499 (1937).

[11] F. S. Pereira, F. F. Grinstein, D. M. Israel, R. Rauenzahn, and S. S. Girimaji, Modeling and simulation of transitional taylor-green vortex flow with partially averaged navier-stokes equations, *Phys. Rev. Fluids* **6**, 054611 (2021).

[12] S. Kida, Three-dimensional periodic flows with high-symmetry, *Journal of the Physical Society of Japan* **54**, 2132 (1985).

[13] O. N. Boratav and R. B. Pelz, Direct numerical simulation of transition to turbulence from a high-symmetry initial condition, *Physics of Fluids* **6**, 2757 (1994).

[14] M. Frigo and S. Johnson, The design and implementation of fftw3, *Proceedings of the IEEE* **93**, 216 (2005).

[15] J. A. Domaradzki and R. S. Rogallo, Local energy transfer and nonlocal interactions in homogeneous, isotropic turbulence, *Physics of Fluids A: Fluid Dynamics* **2**, 413 (1990).

[16] J. Patterson, G. S. and S. A. Orszag, Spectral calculations of isotropic turbulence: Efficient removal of aliasing interactions, *The Physics of Fluids* **14**, 2538 (1971).

[17] C. Canuto, M. Y. Hussaini, A. Quarteroni, and T. A. Zang, Spectral approximation, in *Spectral Methods in Fluid Dynamics* (Springer Berlin Heidelberg, Berlin, Heidelberg, 1988) pp. 31–75.

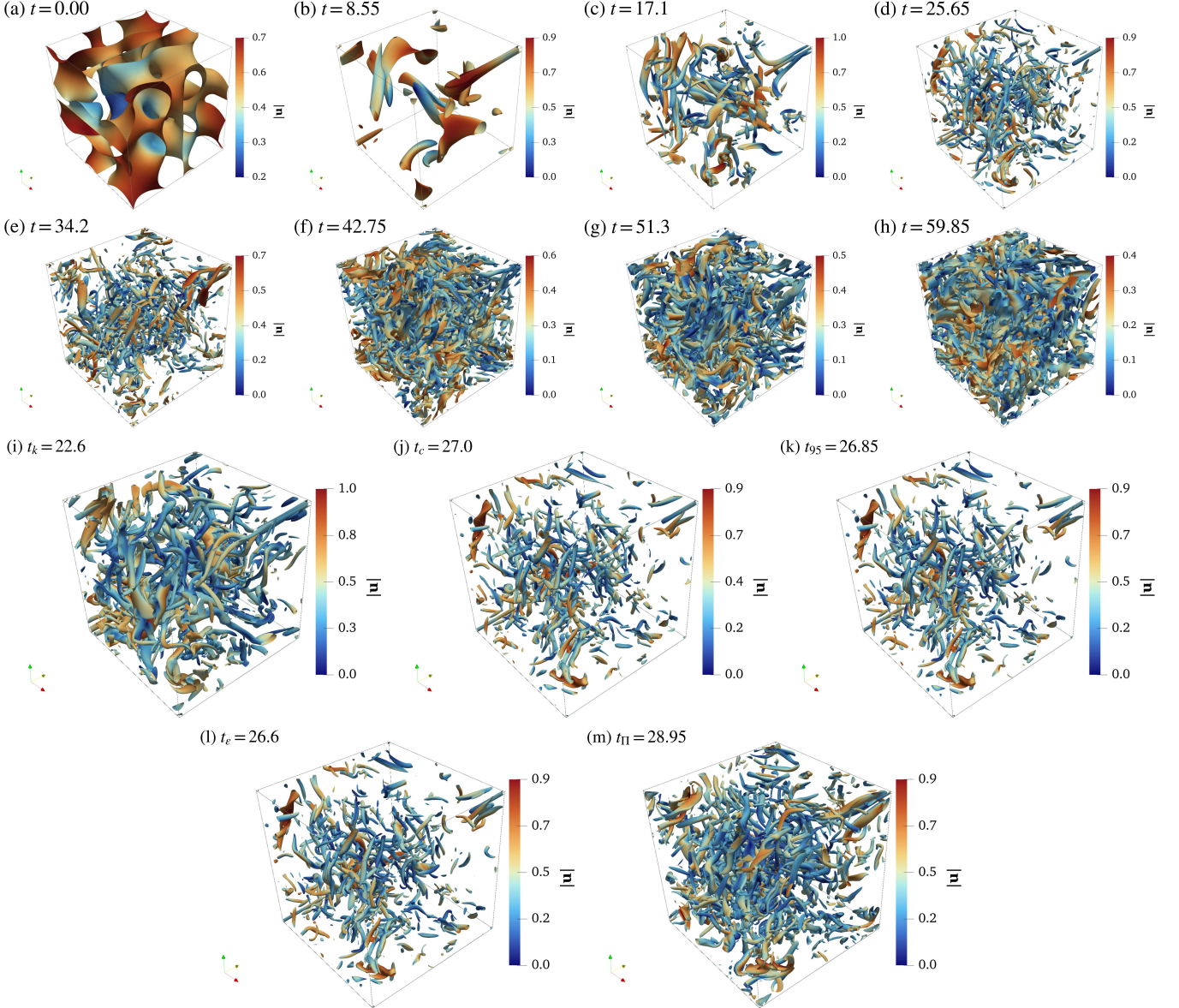


FIG. 1. Q -criterion isosurfaces (colored by $|\mathbf{u}|$) at selected times for the 512^3 Multi-ABC run. Panels (a)–(h) show $t = 0, 8.55, 17.1, 25.65, 34.2, 42.75, 51.3, 59.85$. Panels (i)–(m) show additional snapshots at characteristic times extracted from spectral diagnostics: $t_k = 22.6$, $t_c = 27.0$, $t_{95} = 26.85$, $t_\epsilon = 26.6$, and $t_\Pi = 28.95$ (see Sec. IV for definitions). The isosurface level and rendering settings are the same as in Ref. [9].

- [18] N. J. Higham, Chap. 4. Summation, in *Accuracy and Stability of Numerical Algorithms* (SIAM, Philadelphia, PA, 2002) pp. 79–92.
- [19] D. W. Condiffe and J. S. Dahler, Fluid mechanical aspects of antisymmetric stress, *The Physics of Fluids* **7**, 842 (1964).
- [20] A. Eringen, Simple microfluids, *International Journal of Engineering Science* **2**, 205 (1964).
- [21] A. C. ERINGEN, Theory of micropolar fluids, *Journal of Mathematics and Mechanics* **16**, 1 (1966).
- [22] A. Eringen, Micropolar fluids with stretch, *International Journal of Engineering Science* **7**, 115 (1969).

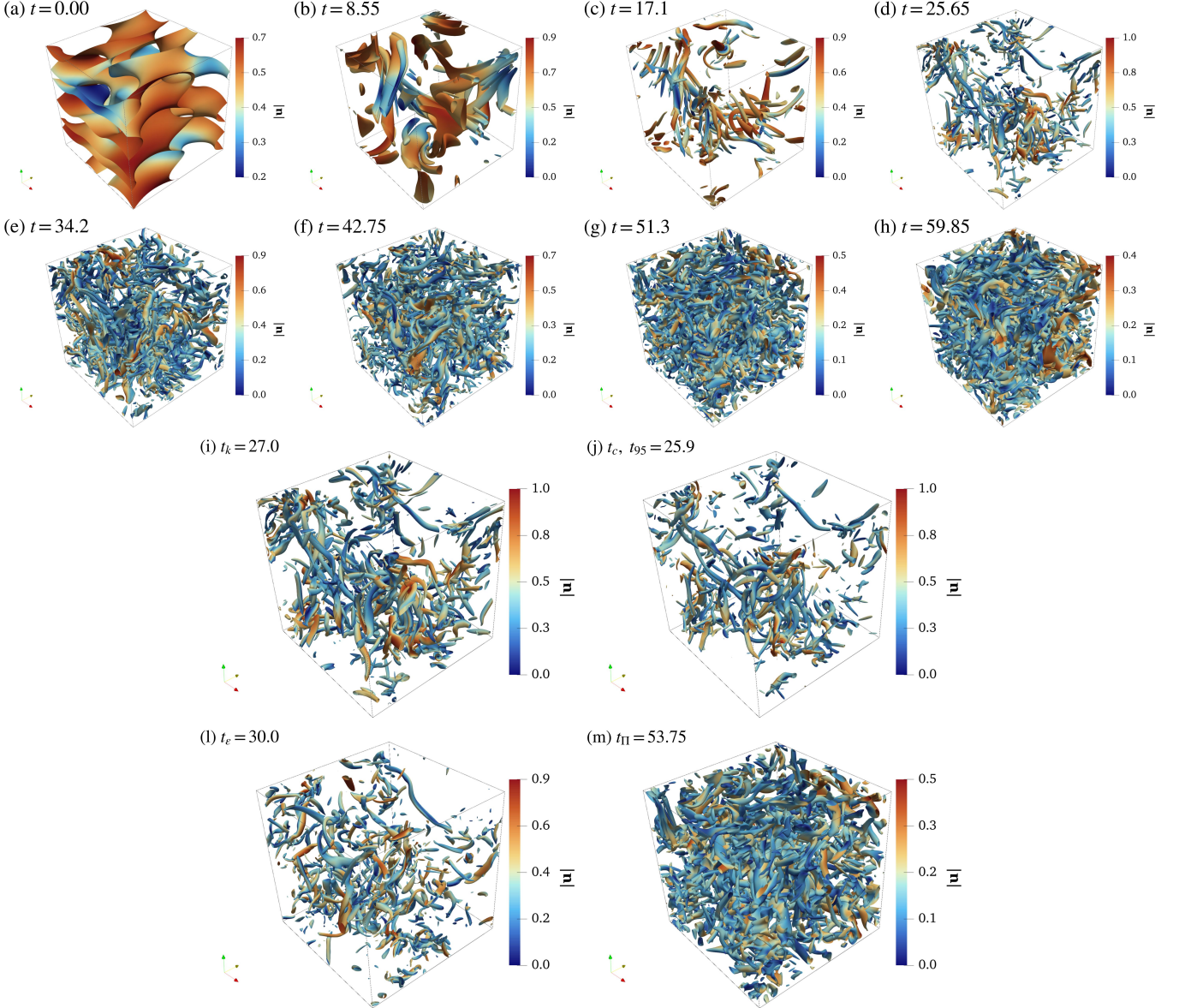


FIG. 2. Q -criterion isosurfaces (colored by $|\mathbf{u}|$) at selected times for the 512^3 Multi-ABC (Asymmetric) run. Panels (a)–(h) show $t = 0, 8.55, 17.1, 25.65, 34.2, 42.75, 51.3, 59.85$. Panels (i)–(m) annotate snapshots at characteristic times: $t_k = 27.0$, $t_c = 30.0$, and $t_{II} = 53.75$ (Sec. IV). Here t_c and t_{95} coincide ($t_c = t_{95} = 25.9$), and the corresponding snapshot is shown in panel (j). The isosurface level and rendering settings are the same as in Ref. [9].

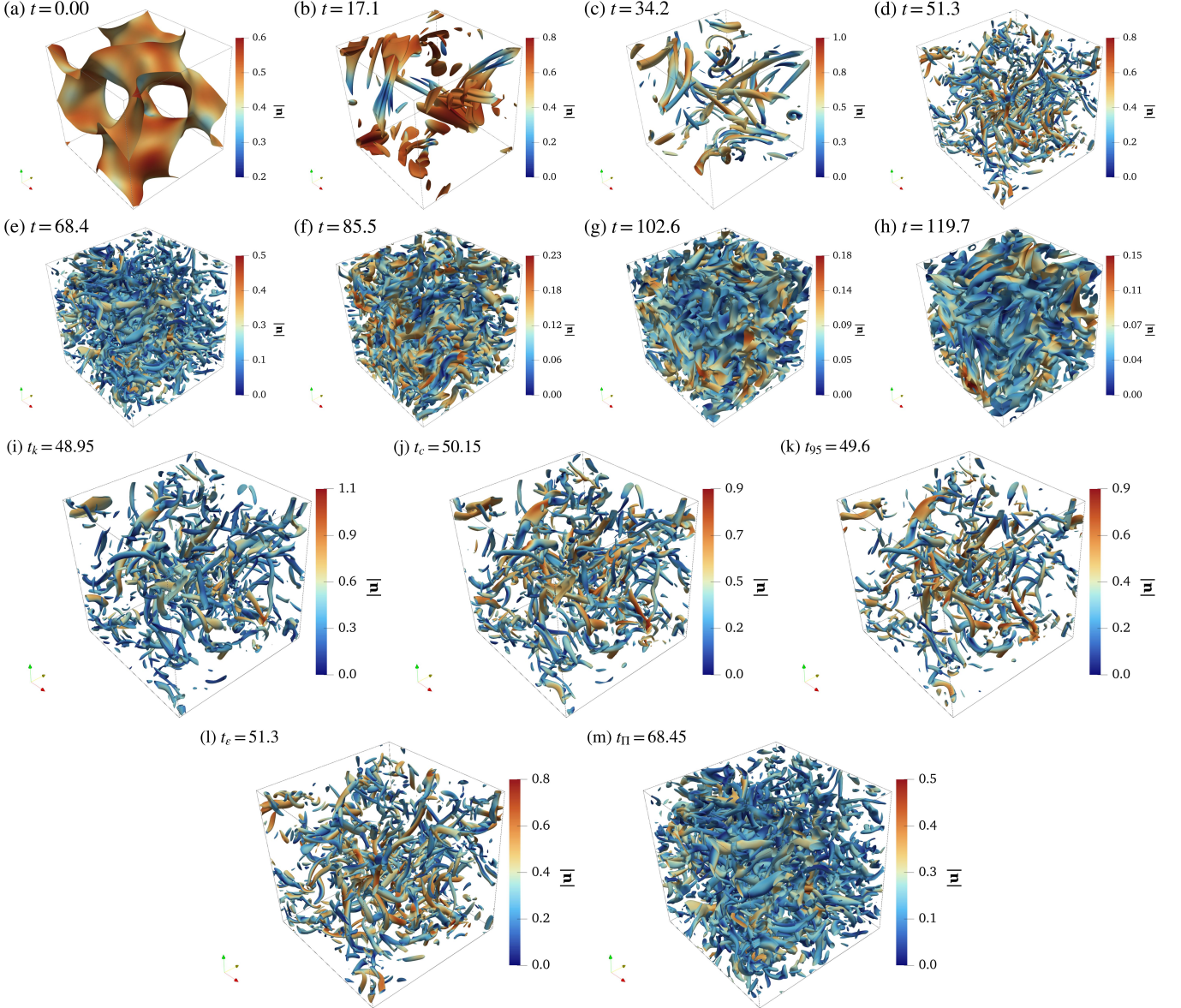


FIG. 3. Q -criterion isosurfaces (colored by $|\mathbf{u}|$) at selected times for the 512^3 ABC+random-phase low- k run. Panels (a)–(h) show $t = 0, 17.1, 34.2, 51.3, 68.4, 85.5, 102.6, 119.7$. Panels (i)–(m) show snapshots at characteristic times: $t_k = 48.95$, $t_c = 50.15$, $t_{95} = 49.6$, $t_\epsilon = 51.3$, and $t_\Pi = 68.45$ (see Sec. IV for definitions). The isosurface level and rendering settings are the same as in Ref. [9].

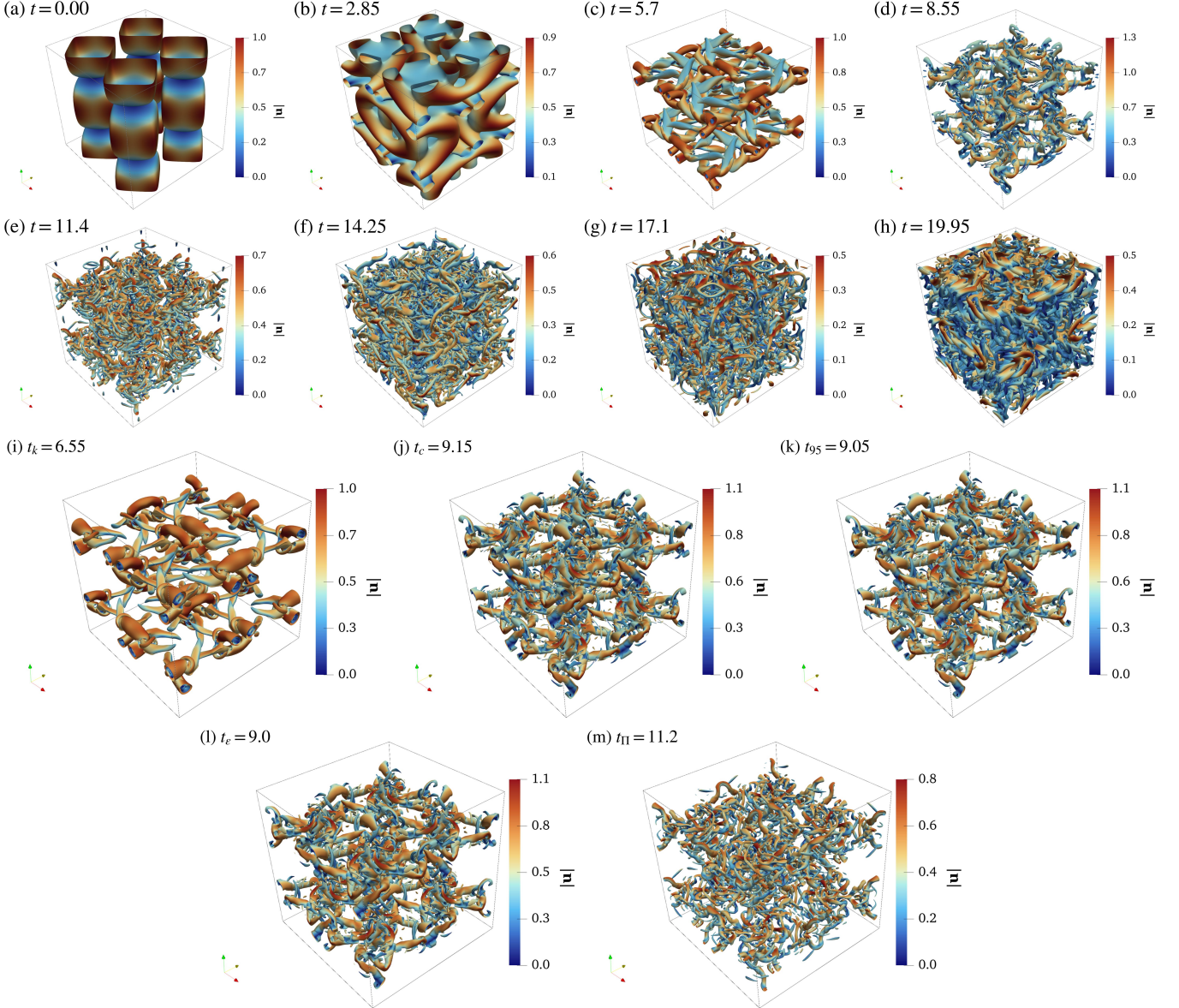


FIG. 4. Q -criterion isosurfaces (colored by $|\mathbf{u}|$) at selected times for the 512^3 Taylor–Green vortex (TGV) run. Panels (a)–(h) show $t = 0, 2.85, 5.7, 8.55, 11.4, 14.25, 17.1, 19.95$. Panels (i)–(m) show snapshots at characteristic times: $t_k = 6.55$, $t_c = 9.15$, $t_{95} = 9.05$, $t_\epsilon = 9.0$, and $t_\Pi = 11.2$ (see Sec. IV for definitions). The isosurface level and rendering settings are the same as in Ref. [9].

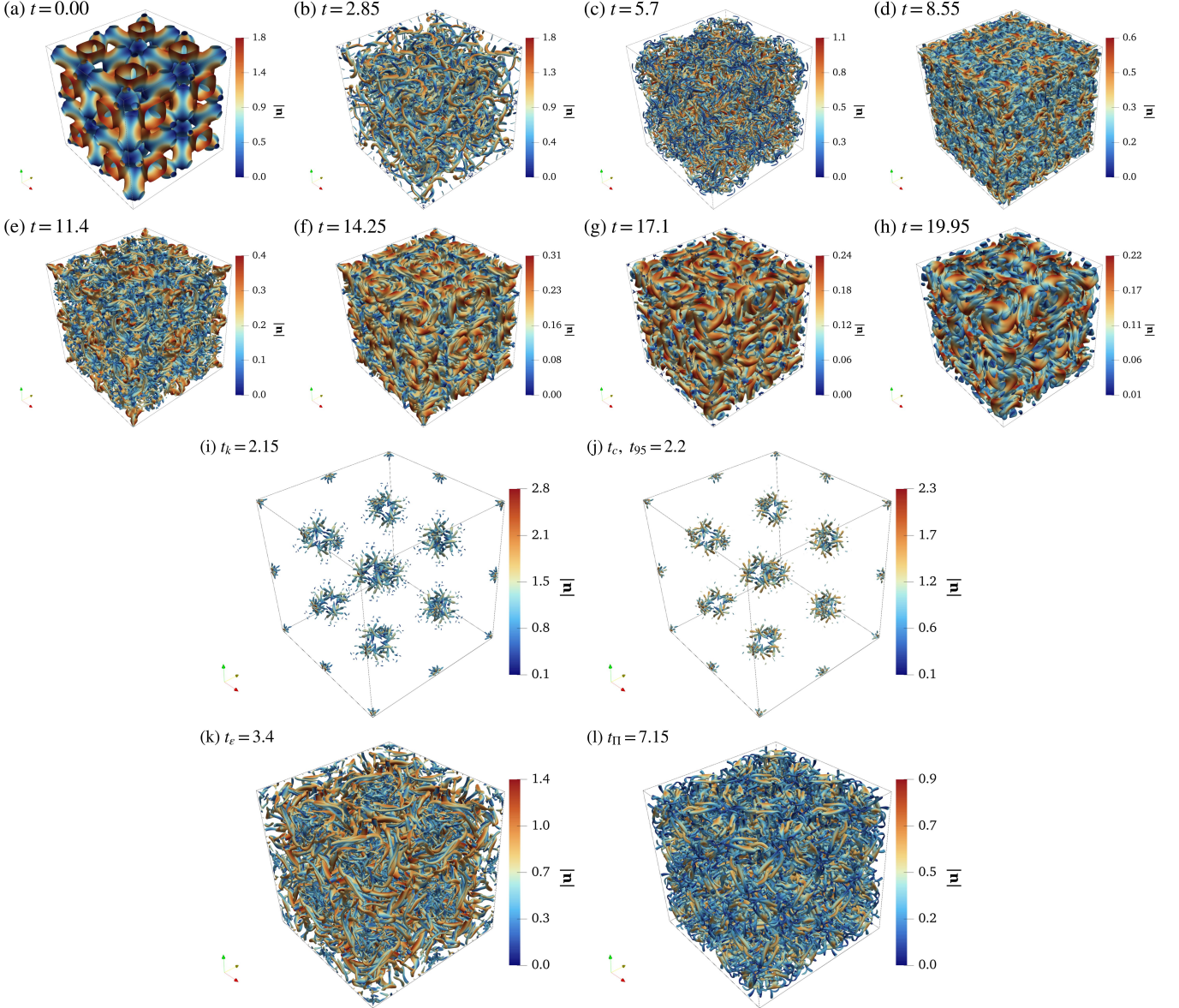


FIG. 5. Q -criterion isosurfaces (colored by $|\mathbf{u}|$) at selected times for the 512^3 Kida–Pelz run. Panels (a)–(h) show $t = 0, 2.85, 5.7, 8.55, 11.4, 14.25, 17.1, 19.95$. Panels (i)–(l) show additional snapshots around the dissipation episode, including the dissipation- and flux-related times $t_\epsilon = 3.4$ and $t_{\text{II}} = 7.15$ (Sec. IV). The 512^3 Kida–Pelz run is shown here to highlight the rapid emergence of fine-scale structures and the resolution sensitivity of peak picking in curvature-weighted spectra; the characteristic times reported for Kida–Pelz in Table I are extracted from the 1024^3 reference simulation (Sec. IV F). The isosurface level and rendering settings are the same as in Ref. [9]. The snapshot labels (e.g., t_k , t_c , t_{95}) correspond to the 512^3 visualization; t_k differs from the 1024^3 reference value due to peak-locking issues, whereas t_ϵ , t_c , t_{95} were confirmed unchanged at 1024^3 (Table II).

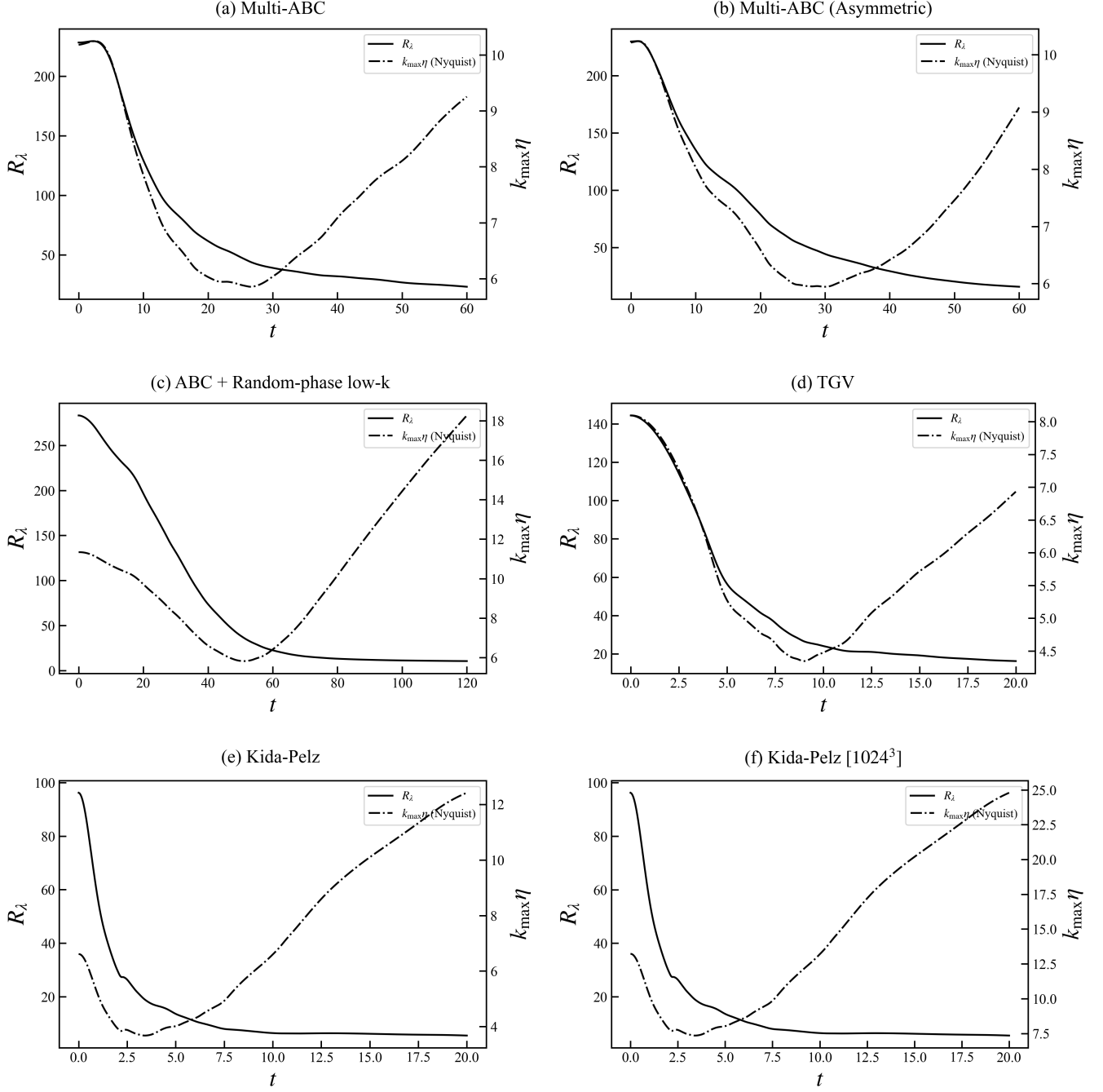


FIG. 6. Resolution diagnostics for the six simulations: time series of the Taylor-microscale Reynolds number $R_\lambda(t)$ (solid line, left axis) and the resolution measure $k_{\max}\eta(t)$ (dash-dotted line, right axis; Nyquist definition $k_{\max} = (N/2)2\pi/L$). Panels correspond to (a) Multi-ABC, (b) Multi-ABC (Asymmetric), (c) ABC+random-phase low- k , (d) TGV, (e) Kida-Pelz (512^3), and (f) Kida-Pelz (1024^3). The Kolmogorov length $\eta(t) = (\nu^3/\varepsilon)^{1/4}$ and $R_\lambda(t)$ are computed from the isotropic spectra as described in Sec. IV.

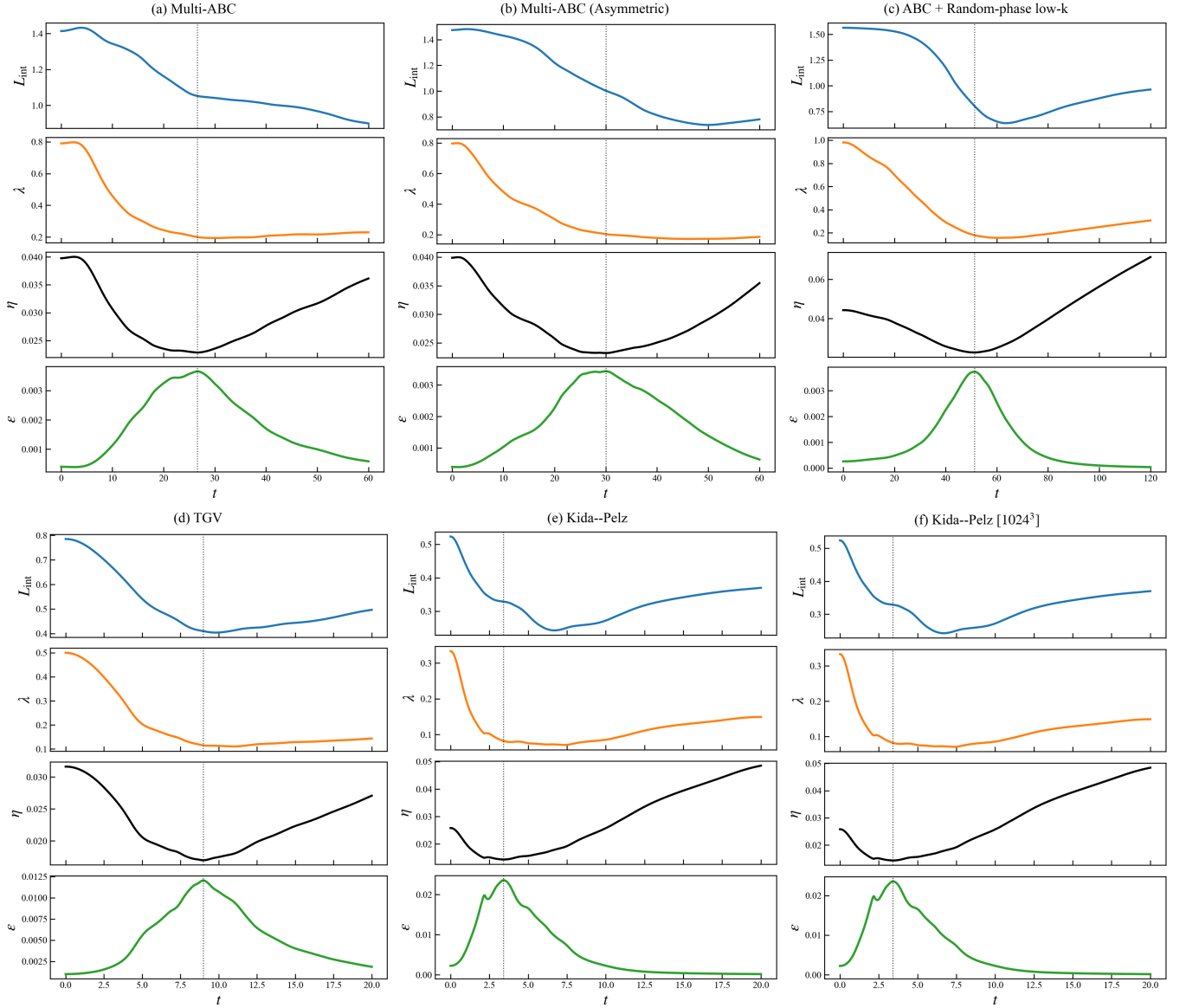


FIG. 7. Time evolution of characteristic length scales and dissipation for all cases: integral scale $L_{\text{int}}(t)$ (top row), Taylor microscale $\lambda(t)$ (second row), Kolmogorov length $\eta(t)$ (third row), and dissipation rate $\varepsilon(t)$ (bottom row), shown for (a) Multi-ABC, (b) Multi-ABC (Asymmetric), (c) ABC+random-phase low- k , (d) TGV, (e) Kida-Pelz (512^3), and (f) Kida-Pelz (1024^3). Vertical dotted lines indicate the dissipation-peak time t_ε for each case. Definitions and spectral evaluation procedures are given in Sec. IV.

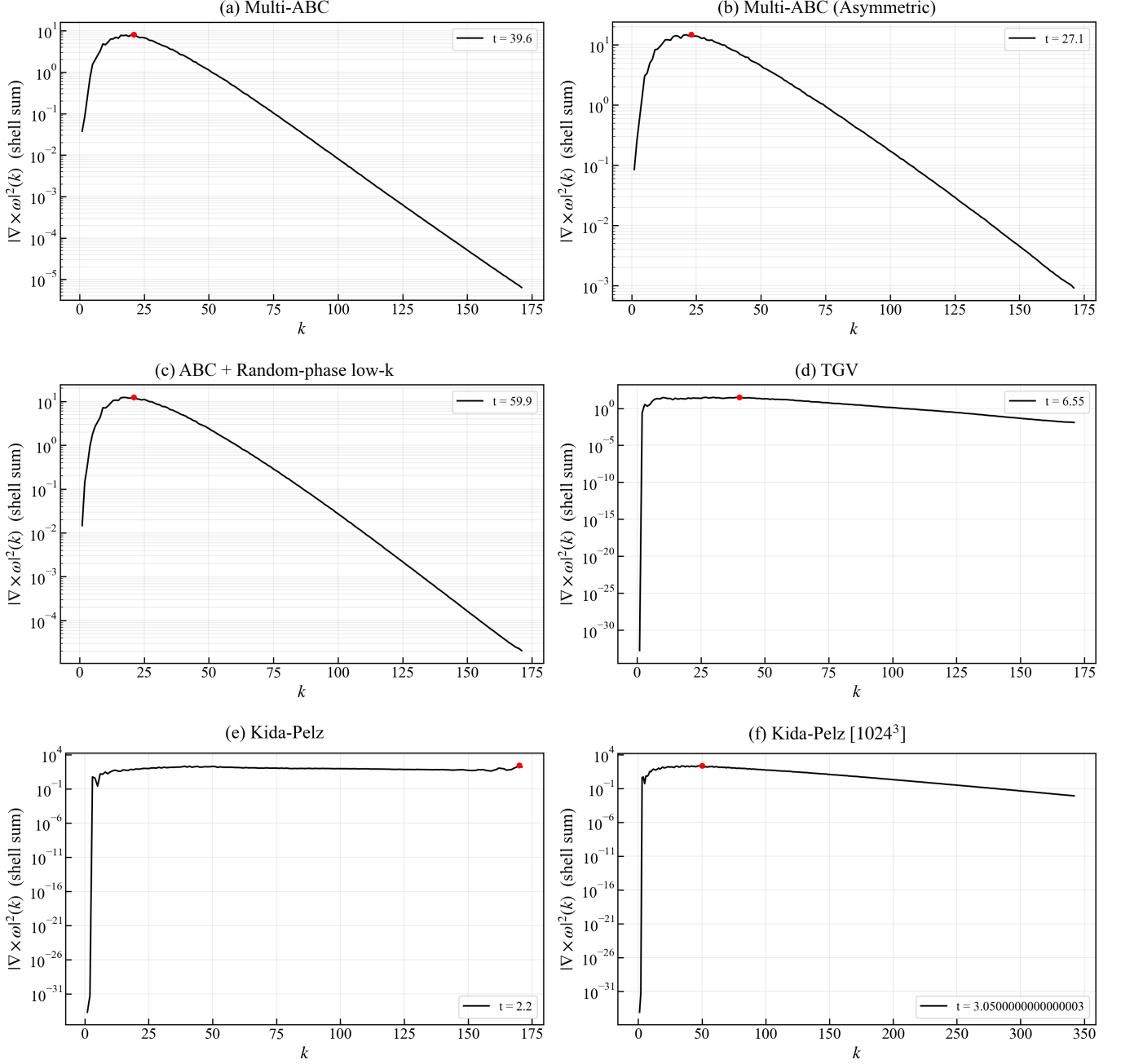


FIG. 8. Inspection of the peak-scale detection based on the curvature-weighted spectrum $|\nabla \times \omega|^2(k)$ (equivalently $k^4 E(k)$ for incompressible flow). Shown are representative shell-summed spectra $|\nabla \times \omega|^2(k)$ at the times indicated in each panel legend for (a) Multi-ABC, (b) Multi-ABC (Asymmetric), (c) ABC+random-phase low- k , (d) TGV, (e) Kida–Pelz (512^3), and (f) Kida–Pelz (1024^3). Red markers denote $k_{\text{peak}} = \arg \max_k \{|\nabla \times \omega|^2(k)\}$. The 512^3 Kida–Pelz case exhibits near-cutoff contamination of the argmax (a spike close to the analysis cutoff $k_{\max}^{(\text{mask})}$), which motivates explicit spike inspection (Sec. IV F) and the higher-resolution 1024^3 run used as the Kida–Pelz reference.

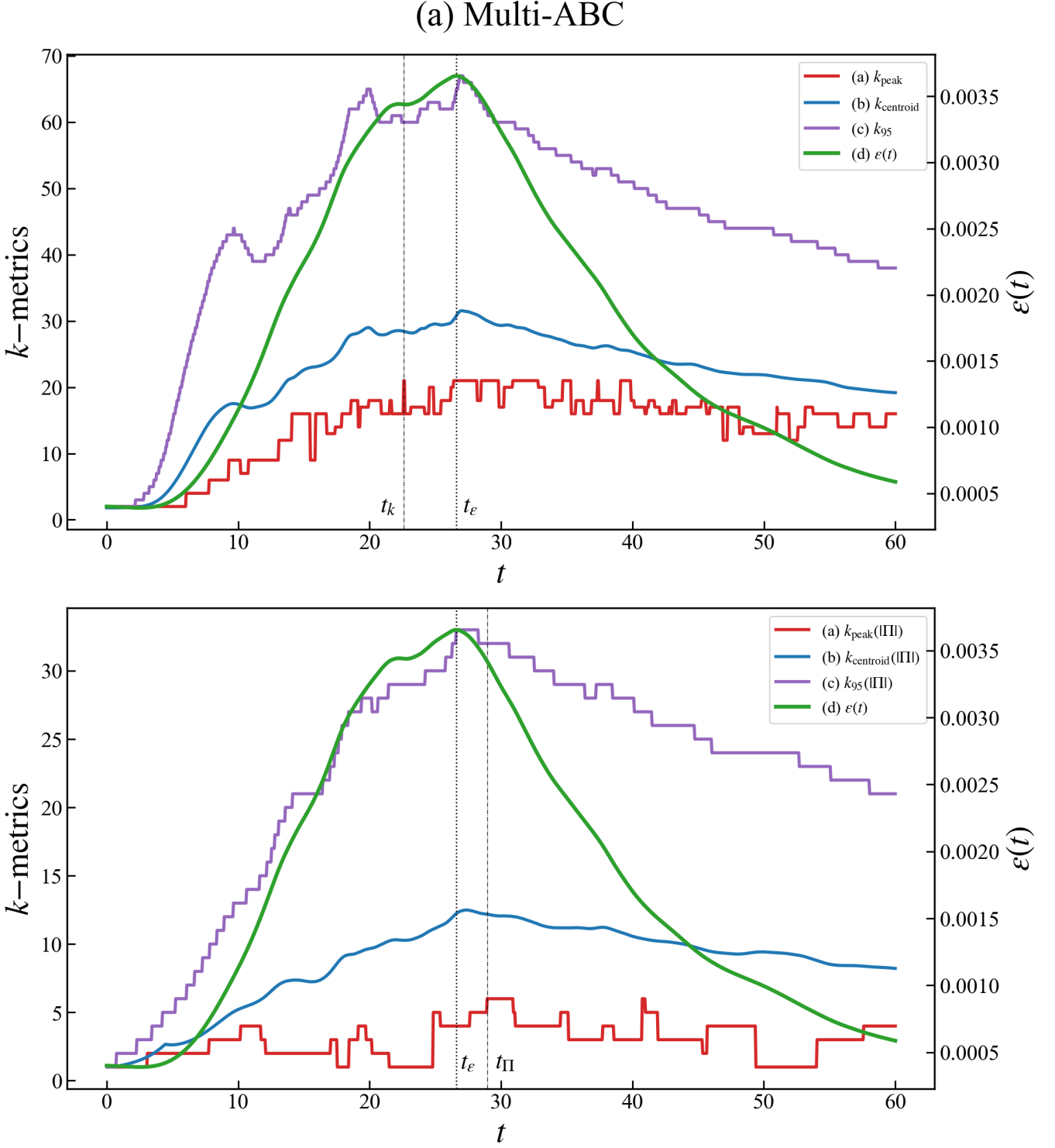


FIG. 9. **Summary of peak/centroid/quantile wavenumber measures and their timing in (a) Multi-ABC.** The upper panel shows characteristic wavenumber measures extracted from the curvature-weighted spectrum $|\nabla \times \omega|^2(k)$ (equivalently $k^4 E(k)$): k_{peak} (red), k_{centroid} (blue), and k_{95} (purple), together with the dissipation rate $\varepsilon(t)$ (green, right axis). The lower panel shows the corresponding measures computed from the flux diagnostic $|\Pi(K)|$ (denoted $k_{\text{peak}}(\Pi)$, $k_{\text{centroid}}(\Pi)$, and $k_{95}(\Pi)$), again with $\varepsilon(t)$ for reference. Vertical markers indicate the characteristic times defined in Sec. IV: $t_k = \arg \max_t k_{\text{peak}}[|\nabla \times \omega|^2](t)$, $t_\varepsilon = \arg \max_t \varepsilon(t)$, and $t_\Pi = \arg \max_t k_{\text{peak}}[|\Pi|](t)$. This combined view enables a direct comparison between (i) the early progression of curvature-weighted small-scale signatures and (ii) the later evolution of interscale transfer, demonstrating the consistent temporal ordering $t_k < t_\varepsilon < t_\Pi$ across all initial conditions.

(b) Multi-ABC (Asymmetric)

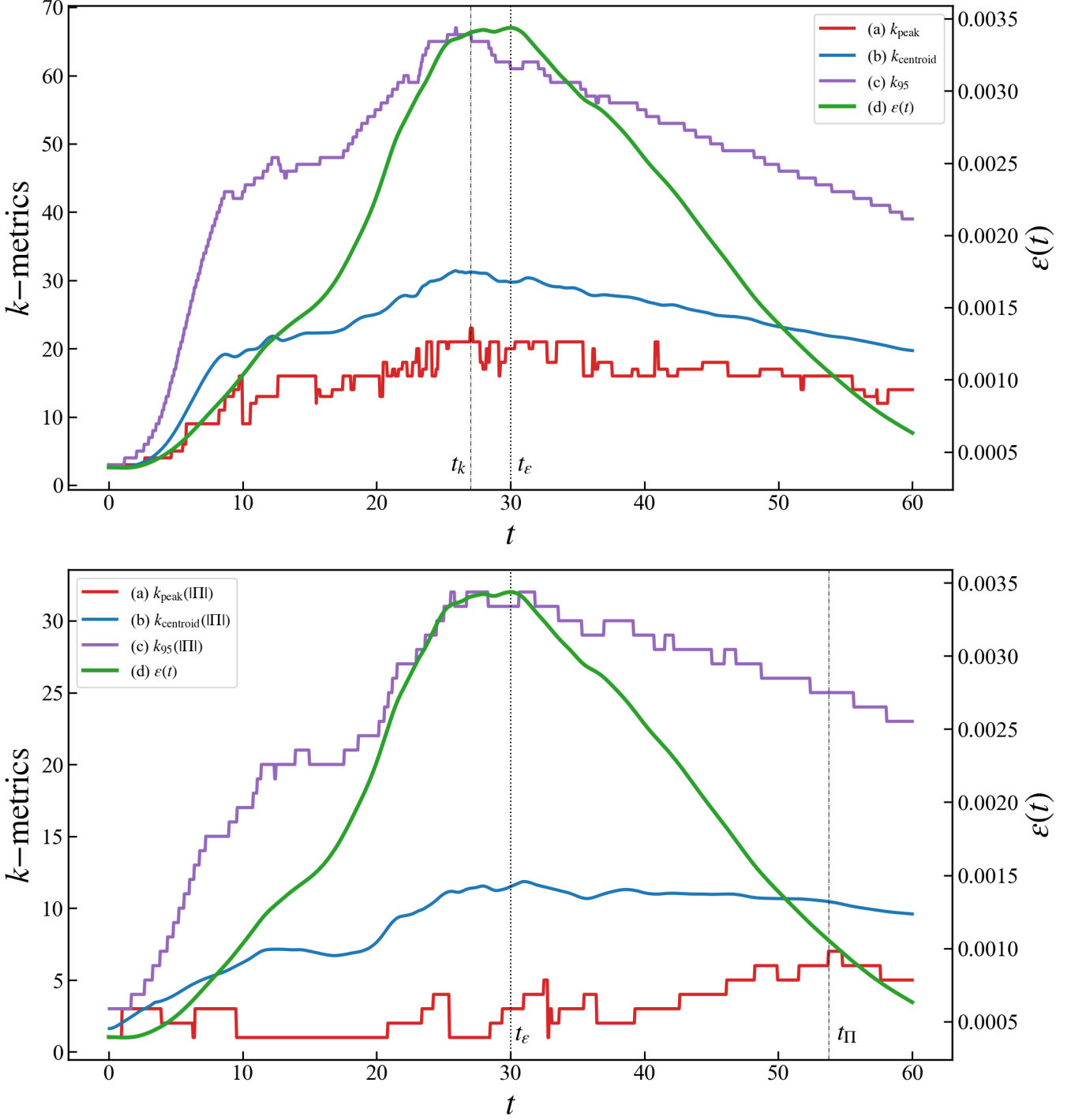


FIG. 10. **Summary of peak/centroid/quantile wavenumber measures and their timing in (b) Multi-ABC (Asymmetric).** The upper panel shows characteristic wavenumber measures extracted from the curvature-weighted spectrum $|\nabla \times \omega|^2(k)$ (equivalently $k^4 E(k)$): k_{peak} (red), k_{centroid} (blue), and k_{95} (purple), together with the dissipation rate $\varepsilon(t)$ (green, right axis). The lower panel shows the corresponding measures computed from the flux diagnostic $|\Pi(K)|$ (denoted $k_{\text{peak}}(\Pi)$, $k_{\text{centroid}}(\Pi)$, and $k_{95}(\Pi)$), again with $\varepsilon(t)$ for reference. Vertical markers indicate the characteristic times defined in Sec. IV: $t_k = \arg \max_t k_{\text{peak}}[|\nabla \times \omega|^2](t)$, $t_\varepsilon = \arg \max_t \varepsilon(t)$, and $t_\Pi = \arg \max_t k_{\text{peak}}[|\Pi|](t)$. This combined view enables a direct comparison between (i) the early progression of curvature-weighted small-scale signatures and (ii) the later evolution of interscale transfer, demonstrating the consistent temporal ordering $t_k < t_\varepsilon < t_\Pi$ across all initial conditions.

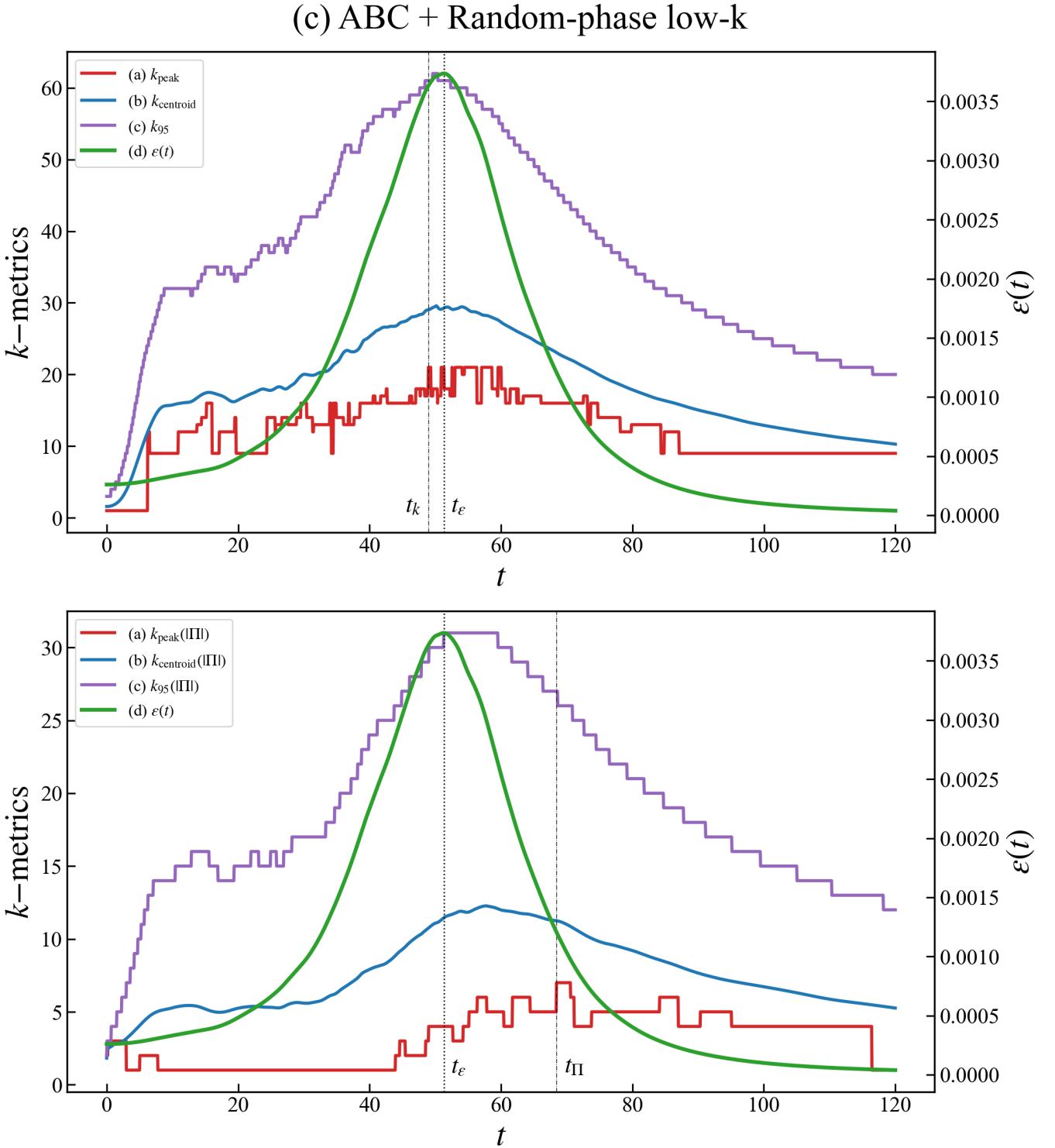


FIG. 11. **Summary of peak/centroid/quantile wavenumber measures and their timing in (c) ABC + random-phase low- k .** The *upper* panel shows characteristic wavenumber measures extracted from the curvature-weighted spectrum $|\nabla \times \omega|^2(k)$ (equivalently $k^4 E(k)$): k_{peak} (red), k_{centroid} (blue), and k_{95} (purple), together with the dissipation rate $\varepsilon(t)$ (green, right axis). The *lower* panel shows the corresponding measures computed from the flux diagnostic $|\Pi(K)|$ (denoted $k_{\text{peak}}(\text{II})$, $k_{\text{centroid}}(\text{II})$, and $k_{95}(\text{II})$), again with $\varepsilon(t)$ for reference. Vertical markers indicate the characteristic times defined in Sec. IV: $t_k = \arg \max_t k_{\text{peak}}[|\nabla \times \omega|^2](t)$, $t_\varepsilon = \arg \max_t \varepsilon(t)$, and $t_\Pi = \arg \max_t k_{\text{peak}}[|\Pi|](t)$. This combined view enables a direct comparison between (i) the early progression of curvature-weighted small-scale signatures and (ii) the later evolution of interscale transfer, demonstrating the consistent temporal ordering $t_k < t_\varepsilon < t_\Pi$ across all initial conditions.

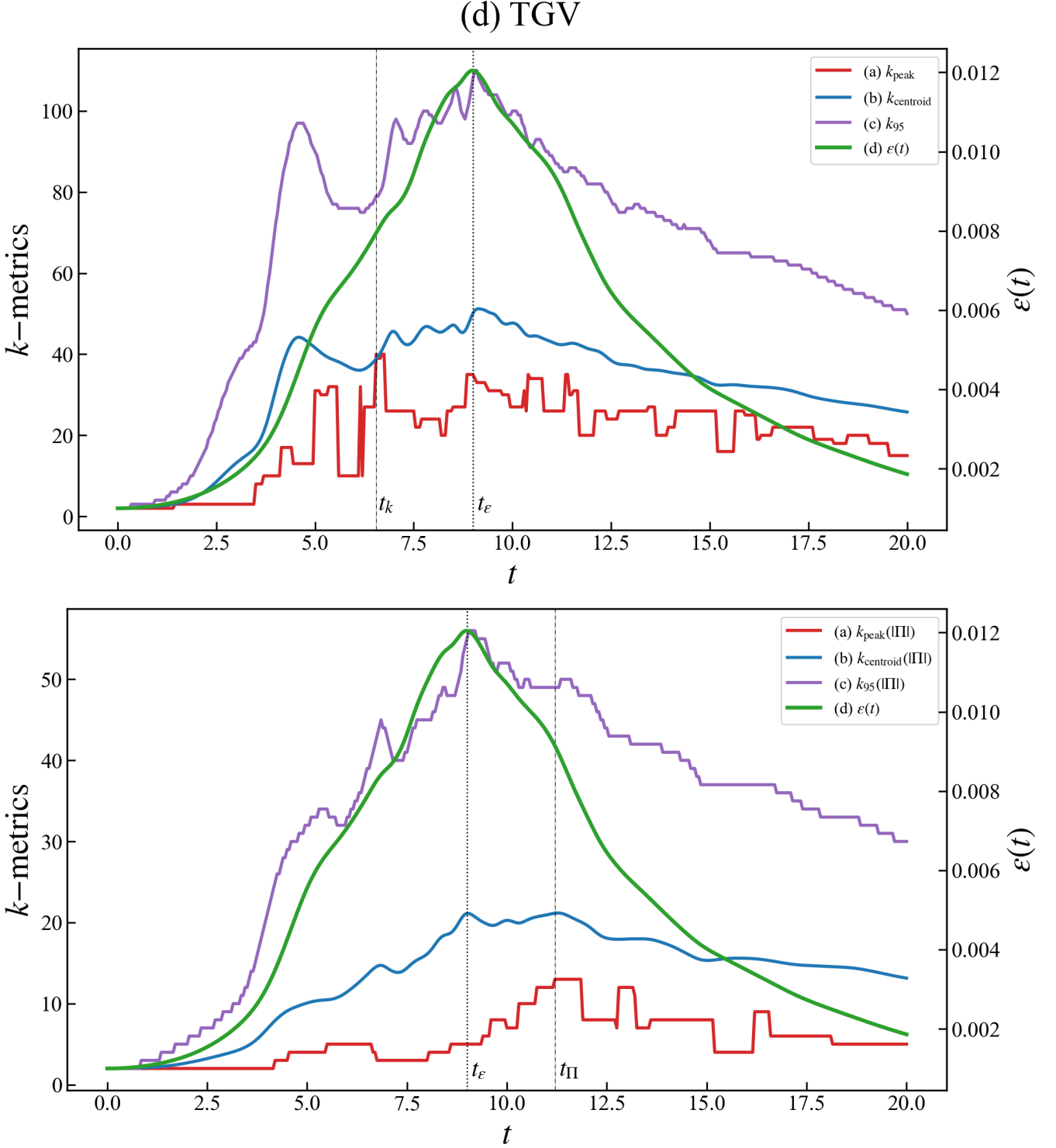


FIG. 12. **Summary of peak/centroid/quantile wavenumber measures and their timing in (d) TGV.** The *upper panel* shows characteristic wavenumber measures extracted from the curvature-weighted spectrum $|\nabla \times \omega|^2(k)$ (equivalently $k^4 E(k)$): k_{peak} (red), k_{centroid} (blue), and k_{95} (purple), together with the dissipation rate $\varepsilon(t)$ (green, right axis). The *lower panel* shows the corresponding measures computed from the flux diagnostic $|\Pi(K)|$ (denoted $k_{\text{peak}}(\text{III})$, $k_{\text{centroid}}(\text{III})$, and $k_{95}(\text{III})$), again with $\varepsilon(t)$ for reference. Vertical markers indicate the characteristic times defined in Sec. IV: $t_k = \arg \max_t k_{\text{peak}}[|\nabla \times \omega|^2](t)$, $t_\varepsilon = \arg \max_t \varepsilon(t)$, and $t_{\Pi} = \arg \max_t k_{\text{peak}}[|\Pi|](t)$. This combined view enables a direct comparison between (i) the early progression of curvature-weighted small-scale signatures and (ii) the later evolution of interscale transfer, demonstrating the consistent temporal ordering $t_k < t_\varepsilon < t_{\Pi}$ across all initial conditions.

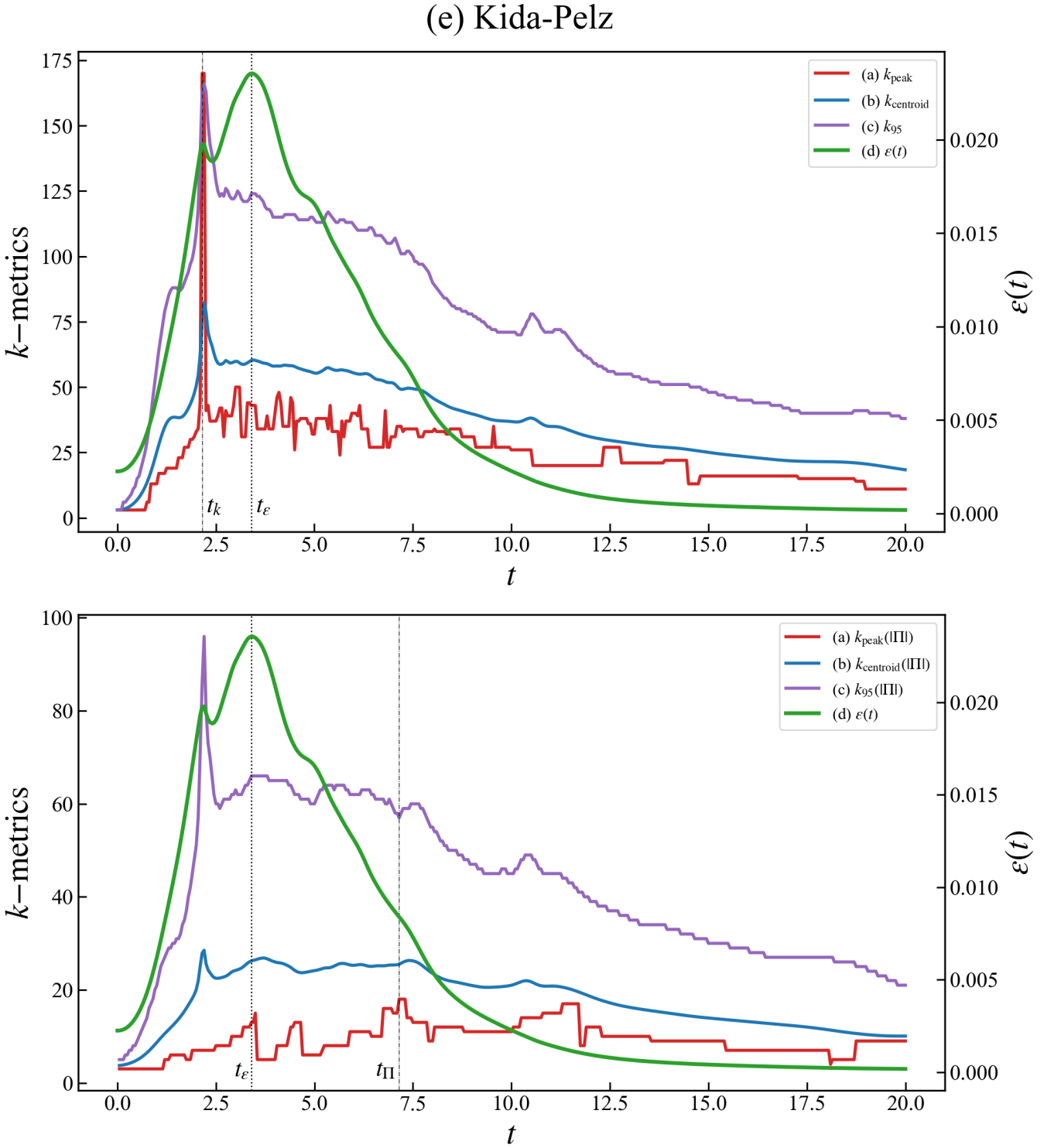


FIG. 13. **Summary of peak/centroid/quantile wavenumber measures and their timing in (e) Kida-Pelz.** The *upper* panel shows characteristic wavenumber measures extracted from the curvature-weighted spectrum $|\nabla \times \omega|^2(k)$ (equivalently $k^4 E(k)$): k_{peak} (red), k_{centroid} (blue), and k_{95} (purple), together with the dissipation rate $\varepsilon(t)$ (green, right axis). The *lower* panel shows the corresponding measures computed from the flux diagnostic $|\Pi(K)|$ (denoted $k_{\text{peak}}(\Pi)$, $k_{\text{centroid}}(\Pi)$, and $k_{95}(\Pi)$), again with $\varepsilon(t)$ for reference. Vertical markers indicate the characteristic times defined in Sec. IV: $t_k = \arg \max_t k_{\text{peak}}[|\nabla \times \omega|^2](t)$, $t_\varepsilon = \arg \max_t \varepsilon(t)$, and $t_\Pi = \arg \max_t k_{\text{peak}}[|\Pi|](t)$. In this 512^3 case, the detected $k_{\text{peak}}[|\nabla \times \omega|^2](t)$ can reach the analysis cutoff $k_{\text{max}}^{(\text{mask})}$ during the early transient (endpoint hit), reflecting cutoff-proximate peak locking; panel (f) (1024^3) shows the resolved reference behavior without such locking (cf. Fig. 8).

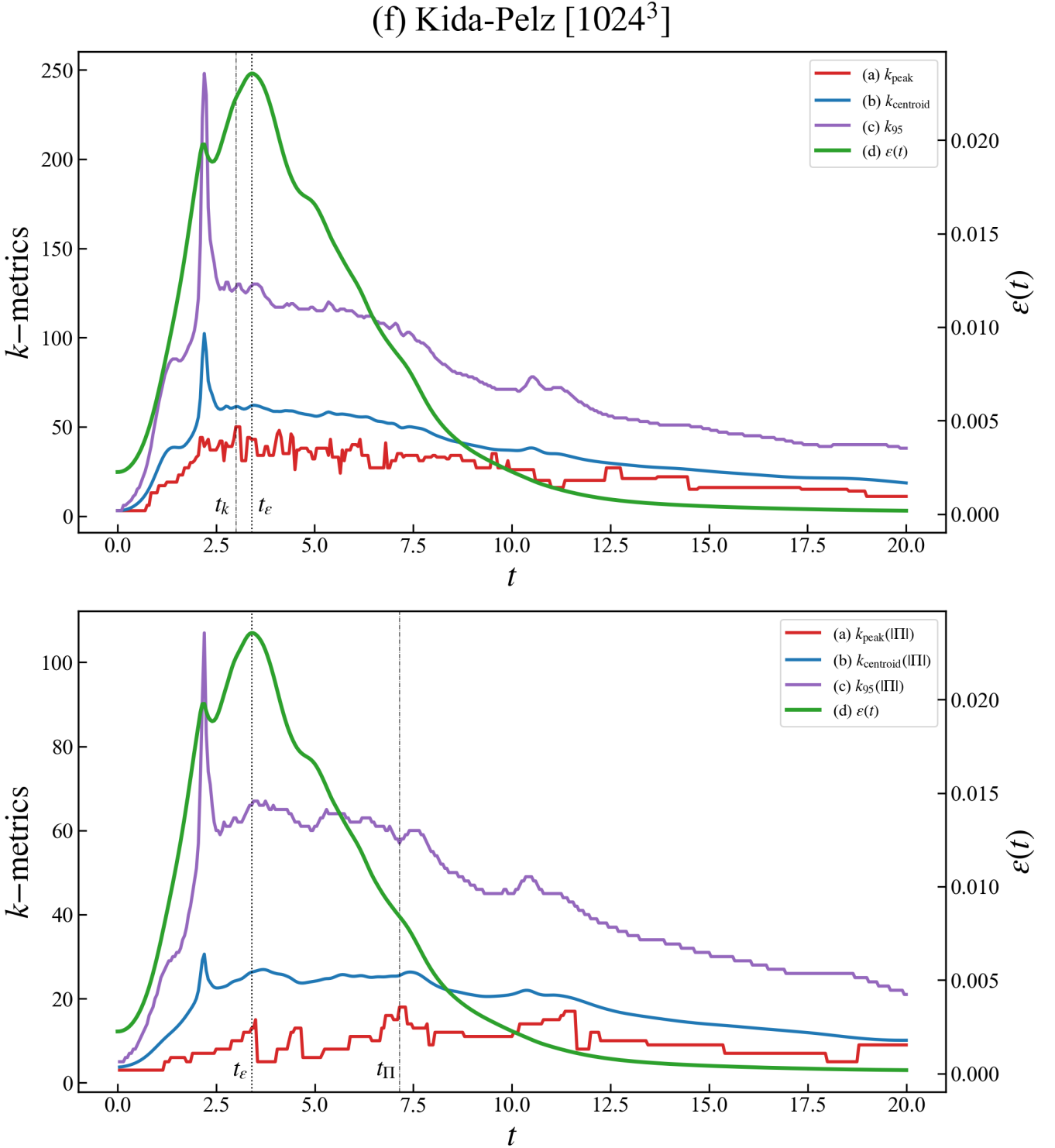


FIG. 14. **Summary of peak/centroid/quantile wavenumber measures and their timing in (f) Kida-Pelz $[1024^3]$.** The upper panel shows characteristic wavenumber measures extracted from the curvature-weighted spectrum $|\nabla \times \boldsymbol{\omega}|^2(k)$ (equivalently $k^4 E(k)$): k_{peak} (red), k_{centroid} (blue), and k_{95} (purple), together with the dissipation rate $\varepsilon(t)$ (green, right axis). The lower panel shows the corresponding measures computed from the flux diagnostic $|\Pi(K)|$ (denoted $k_{\text{peak}}(\Pi)$, $k_{\text{centroid}}(\Pi)$, and $k_{95}(\Pi)$), again with $\varepsilon(t)$ for reference. Vertical markers indicate the characteristic times defined in Sec. IV: $t_k = \arg \max_t k_{\text{peak}}[|\nabla \times \boldsymbol{\omega}|^2](t)$, $t_\varepsilon = \arg \max_t \varepsilon(t)$, and $t_{\Pi} = \arg \max_t k_{\text{peak}}[|\Pi|](t)$. This combined view enables a direct comparison between (i) the early progression of curvature-weighted small-scale signatures and (ii) the later evolution of interscale transfer, demonstrating the consistent temporal ordering $t_k < t_\varepsilon < t_{\Pi}$ across all initial conditions.

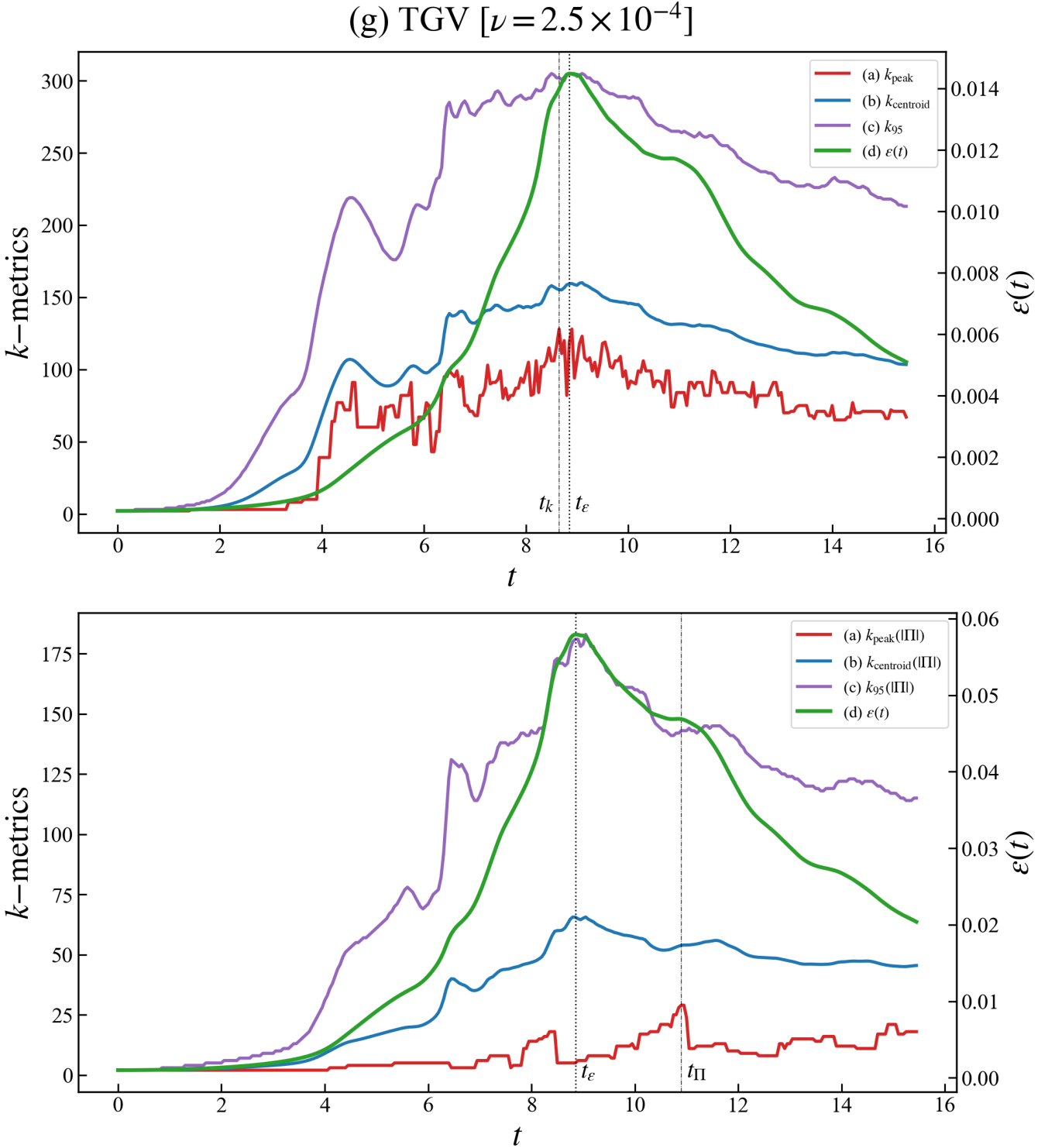


FIG. 15. Viscosity variation in Taylor-Green vortex flow: low-viscosity case $\nu = 2.5 \times 10^{-4}$ (reference resolution $N^3 = 1024^3$). The *upper* panel shows the time series of peak-based wavenumber measures of the curvature-weighted spectrum $|\nabla \times \omega|^2(k)$: k_{peak} , k_{centroid} , and k_{95} , together with $\varepsilon(t)$. Vertical markers indicate $t_k = \arg \max_t k_{\text{peak}}(t)$ and the dissipation peak time t_ε . The *lower* panel shows the peak-based measures for the nonlinear energy-flux spectrum $|\Pi(K)|$, with $t_\Pi = \arg \max_t k_{\text{peak}}[|\Pi|](t)$. The ordering $t_k < t_\varepsilon < t_\Pi$ remains intact at this lower viscosity.

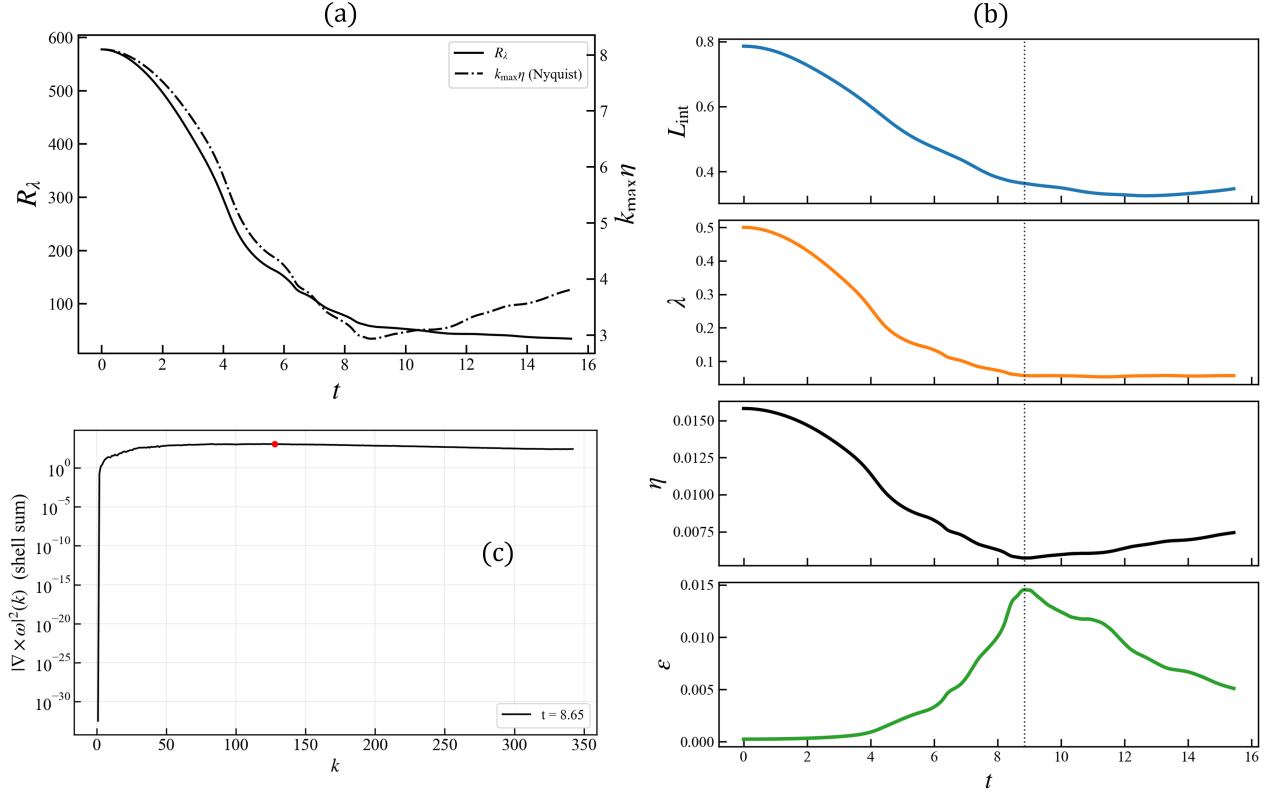


FIG. 16. Viscosity variation in Taylor-Green vortex flow: low-viscosity case $\nu = 2.5 \times 10^{-4}$ (reference resolution $N^3 = 1024^3$). (a) Resolution and Reynolds-number diagnostics $R_\lambda(t)$ and $k_{\max}\eta(t)$. (b) Integral, Taylor, and Kolmogorov scales and the dissipation rate. (c) Inspection of $|\nabla \times \omega|^2(k)$ at $t = t_k$, showing a well-defined peak away from the cutoff (cf. Sec. V F).

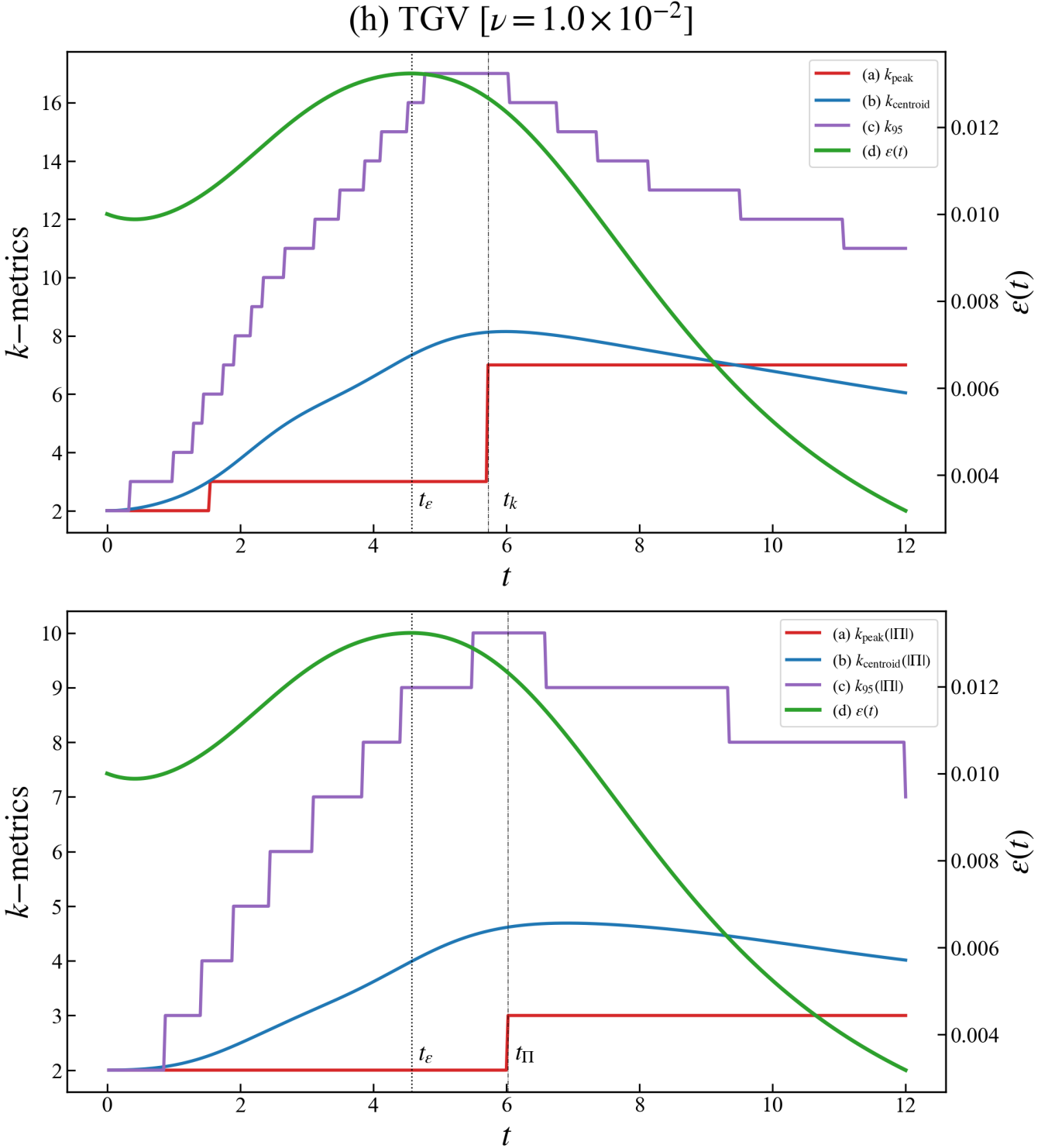


FIG. 17. Viscosity variation in Taylor–Green vortex flow: high-viscosity case $\nu = 10^{-2}$ ($N^3 = 512^3$). Same layout as Fig. 15. At this viscosity the dissipation peak precedes the maximum-attainment time of the curvature-weighted peak scale, $t_\varepsilon < t_k$, illustrating a viscosity-dependent breakdown of the ordering observed in the baseline cases.

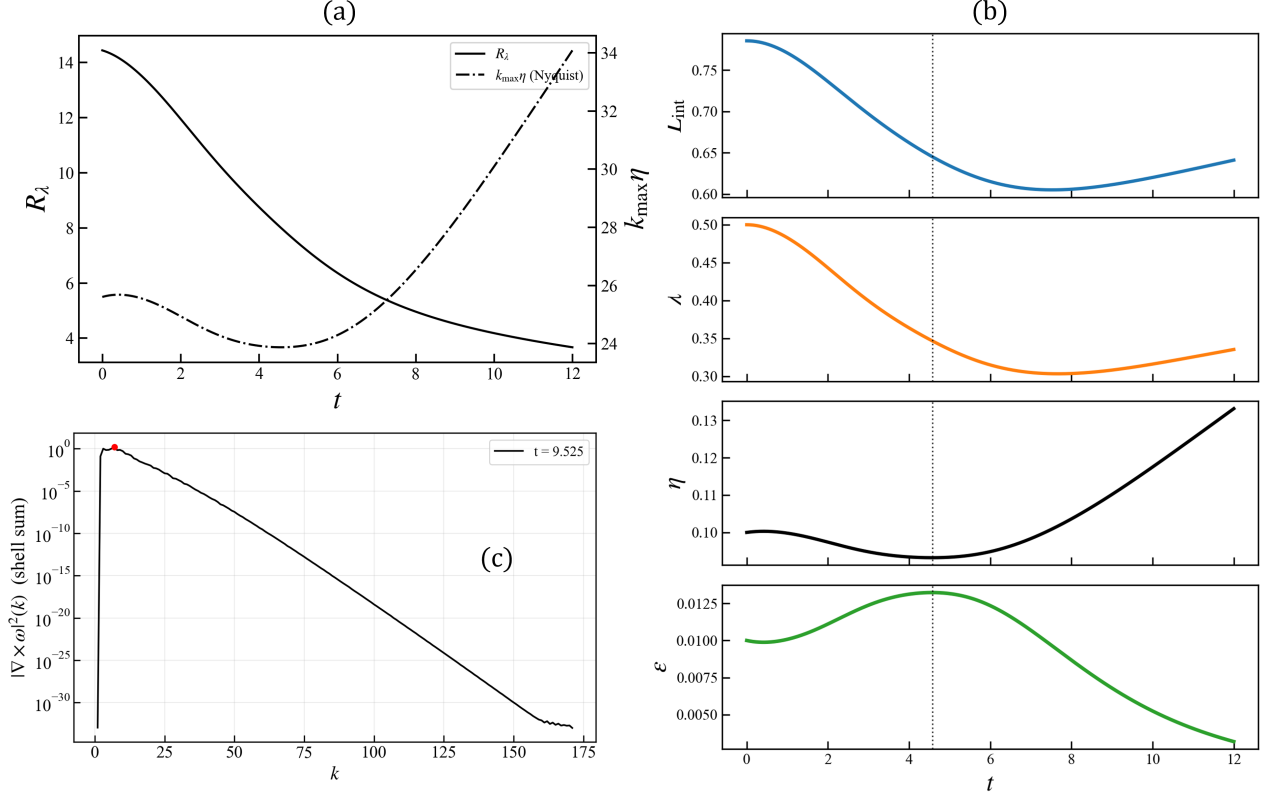


FIG. 18. Viscosity variation in Taylor-Green vortex flow: high-viscosity case $\nu = 10^{-2}$ ($N^3 = 512^3$). Same layout as Fig. 16.